

Article

Phosphotungstic Acid-Modified MnO_x for Selective Catalytic Reduction of NO_x with NH_3

Hongyan Xue ^{1,2}, Xiaoming Guo ², Dongsen Mao ^{2,*} , Tao Meng ^{1,2} , Jun Yu ² and Zhen Ma ^{1,3,*} 

¹ Shanghai Key Laboratory of Atmospheric Particle Pollution and Prevention (LAP3), Department of Environmental Science and Engineering, Fudan University, Shanghai 200433, China

² Research Institute of Applied Catalysis, School of Chemical and Environmental Engineering, Shanghai Institute of Technology, Shanghai 201418, China

³ Shanghai Institute of Pollution Control and Ecological Security, Shanghai 200092, China

* Correspondence: dsmao@sit.edu.cn (D.M.); zhenma@fudan.edu.cn (Z.M.)

Abstract: $\text{H}_3\text{PW}_{12}\text{O}_{40}$ -modified MnO_x catalysts (denoted as Mn-HPW) were used for NO_x elimination with co-fed NH_3 . The optimal Mn-HPW_{0.02} catalyst exhibited over 90% NO_x conversion at 90–270 °C. The incorporation of HPW increased the amount of Lewis acid sites of the catalyst for adsorbing NH_3 , and accelerated the reaction between the adsorbed NH_3 species and gas-phase NO_x , thus, increasing the low-temperature catalytic activity. The oxidation ability of the Mn catalyst was decreased due to the addition of HPW, thus, mitigating the overoxidation of the adsorbed NH_3 species and improving the de- NO_x activity and N_2 selectivity in the high-temperature region. DRIFT results revealed that the NH_3 species on Lewis and Brønsted acid sites, bridged nitrate, and bidentate nitrate were important species/intermediates for the reaction. NH_3 -SCR over the Mn and Mn-HPW_{0.02} catalysts obeyed the Eley–Rideal and Langmuir–Hinshelwood mechanisms, simultaneously, at 120 °C.

Keywords: MnO_x ; phosphotungstic acid; NH_3 -SCR; NO_x ; catalytic removal



Citation: Xue, H.; Guo, X.; Mao, D.; Meng, T.; Yu, J.; Ma, Z. Phosphotungstic Acid-Modified MnO_x for Selective Catalytic Reduction of NO_x with NH_3 . *Catalysts* **2022**, *12*, 1248. <https://doi.org/10.3390/catal12101248>

Academic Editor: Zhaoyang Fan

Received: 28 September 2022

Accepted: 12 October 2022

Published: 16 October 2022

Publisher's Note: MDPI stays neutral with regard to jurisdictional claims in published maps and institutional affiliations.



Copyright: © 2022 by the authors. Licensee MDPI, Basel, Switzerland. This article is an open access article distributed under the terms and conditions of the Creative Commons Attribution (CC BY) license (<https://creativecommons.org/licenses/by/4.0/>).

1. Introduction

Nitrogen oxides (NO_x) contribute to environmental problems, including photochemical smog and acid rain. Moreover, NO_x facilitates the formation of secondary aerosols and fine particulate matters [1]. Hence, it is important to use efficient technology to eliminate NO_x . Among various de- NO_x technologies, selective catalytic reduction of NO_x using NH_3 (NH_3 -SCR) has been employed extensively, and its decisive factor is the performance of catalysts [2–5].

Mn-based catalysts have been researched extensively for NH_3 -SCR [6–9]. However, MnO_x usually has low surface areas and can achieve high NO_x conversion only in narrow temperature windows [5,10]. In order to improve the catalytic efficiency, MnO_x can be deposited onto TiO_2 [11–13], Al_2O_3 [14–16], carbon [17–19], and zeolites [20–22] that can enhance the dispersion of MnO_x and lead to synergistic effects between MnO_x and the supports. Additionally, the SCR activity of MnO_x is promoted by modification with metal oxides, such as CeO_x [23–26], FeO_x [27–29], CoO_x [9,30,31], NiO_x [32–34], and WO_x [35,36]. For instance, Xu et al. [35] loaded MnO_x - CeO_2 onto WO_3 - ZrO_2 , and the optimal catalyst exhibited above 80% NO conversion at 150–380 °C. The de- NO_x activity, N_2 selectivity, and SO_2 tolerance on MnFe/Ti can be enhanced by doping W [36]. The generation of Mn-O-W and Fe-O-W bonds facilitates the transport of electrons and oxygen, thus, accelerating the SCR reaction. Liu et al. [37] prepared ternary (Mn-Ce-Ti) and binary (Mn-Ti and Ce-Ti) catalysts using a hydrothermal method. The results of de- NO_x activity evaluation illustrate that Mn-Ce-Ti exhibits excellent NH_3 -SCR activity and a strong resistance against H_2O and SO_2 , which is mainly attributed to the dual redox cycle ($\text{Mn}^{4+} + \text{Ce}^{3+} \leftrightarrow \text{Mn}^{3+} + \text{Ce}^{4+}$, $\text{Mn}^{4+} + \text{Ti}^{3+} \leftrightarrow \text{Mn}^{3+} + \text{Ti}^{4+}$) and the amorphous structure. Additionally, metal–organic

frameworks (MOFs)-derived metal oxides possess high porosity and large specific surface areas, profiting from the introduction and dispersion of Bronsted acid sites, thus, enhancing the SCR activity of the Mn-based catalysts [30,38–40].

Tungstophosphoric acid ($\text{H}_3\text{PW}_{12}\text{O}_{40}$, HPW) is composed of bridging metal atoms and oxygen atoms, and exhibits good redox properties, strong acidity, and good thermal stability, which is favorable for the SCR reaction. Thus, HPW-modified SCR catalysts such as HPW/ Fe_2O_3 [41–44], HPW/ CeO_2 [45–47], HPW-Cu-Ti [48], HPW-Fe-Ti [48], HPW- $\text{V}_2\text{O}_5/\text{TiO}_2$ [49], and HPW-Mn-Ce-Co [50] have been developed. For instance, Wu et al. [44] prepared HPW/ Fe_2O_3 by impregnation, and they found that 100% NO conversion at 240–460 °C can be attained on HPW/ Fe_2O_3 -350-0.5. The introduction of HPW enriches the number of acid sites, thus, enhancing NH_3 adsorption. Meanwhile, the oxidation ability of Fe_2O_3 is decreased by adding HPW, thereby inhibiting the overoxidation of NH_3 . Geng et al. [46] developed HPW/ CeO_2 , and they reported that HPW could allow for NH_3 adsorption, while CeO_2 could activate the adsorbed NH_3 and NO species. Thus, superior catalytic activity was obtained on HPW/ CeO_2 . Tang et al. [50] discovered that adsorption and activation of NH_3 were boosted with the introduction of HPW to Mn-Ce-Co-O, and HPW can weaken the influence of SO_2 on active bidentate nitrate, and restrain the formation of metal sulfate, thereby achieving good SO_2 resistance of the catalyst. However, to the best of our knowledge, HPW-modified MnO_x for NH_3 -SCR was not reported.

Herein, Mn-HPW composite catalysts were prepared and the effects of adding HPW to the catalytic performance were evaluated. Furthermore, the correlation between SCR performance and physicochemical properties was researched in detail. The evolution process of NH_3 - and NO_x -derived species over the Mn and Mn-HPW_{0.02} catalysts was monitored at 60–300 °C using DRIFT, and the possible reaction mechanisms at 120 °C were revealed.

2. Results and Discussion

2.1. Textural and Structural Properties

2.1.1. XRD

XRD patterns of the Mn and Mn-HPW_x samples are given in Figure 1. The Mn catalyst shows MnO_2 (PDF # 44-0141), Mn_5O_8 phases (PDF # 39-1218), and Mn_2O_3 (PDF # 41-1442) [51–53], corresponding to the standard pattern in Figure S1. As shown in Figure S2, HPW calcinated at 400 °C shows the peaks of $\text{H}_3\text{PW}_{12}\text{O}_{40}\cdot 6\text{H}_2\text{O}$ (PDF # 50-0304), coinciding with the phenomenon reported by Geng et al. [46] and Wu et al. [44]. For all Mn-HPW_x catalysts, the peak intensities of Mn_2O_3 and Mn_5O_8 decline gradually with the increase of x, and the characteristic peak of HPW is not detected due to the lower content [47]. However, as the x is higher than 0.01, weak peaks of the WO_3 species (PDF # 41-1315) and the MnWO_4 phase (PDF # 13-0434) are detected, due to the partial decomposition of HPW during calcination [54,55]. Characteristic peaks of Mn-HPW_{0.02}, calcinated at different temperatures, are shown in Figure S3, and the phases of MnWO_4 and WO_3 are distinct in Mn-HPW_{0.02} calcinated at 650 °C.

2.1.2. FTIR

FTIR spectra of HPW calcinated at different temperatures are shown in Figure 2. The evident bands of Keggin anion vibration appear at 1080, 980, 890, and 795 cm^{-1} on HPW before calcination and HPW calcinated at 400 °C (Figure 2 in (a,b), and these bands can be ascribed to P-O_a (1080 cm^{-1}) in the central tetrahedra PO_4 , W=O_d (980 cm^{-1}) in terminal oxygens linked to a lone tungsten atom, $\text{W-O}_b\text{-W}$ (890 cm^{-1}) connecting two different W_3O_{13} groups, and the $\text{W-O}_c\text{-W}$ (795 cm^{-1}) vibrations of the same W_3O_{13} groups, respectively [54,55]. However, the bands of W=O_d , $\text{W-O}_b\text{-W}$, and $\text{W-O}_c\text{-W}$ are not detected in HPW calcinated 650 °C (Figure 2 in (c), due to the destruction of the HPW structure. For Mn-HPW_{0.02} before calcination, Mn-HPW_{0.02} calcinated at 200 °C, and Mn-HPW_{0.02} calcined at 400 °C (Figure 2 in (d–f), the characteristic bands of PO_4 , W=O_d , and $\text{W-O}_b\text{-W}$ are evident, although the positions migrate to lower wavenumbers. Especially, the bands of

W-O_c-W are invisible. These phenomena reveal that the structure of HPW is influenced, to some extent, during the preparation. Mn-HPW_{0.02} calcinated at 650 °C shows no obvious bands of HPW, indicating the decomposition of HPW at 650 °C (Figure 2 in (g)).

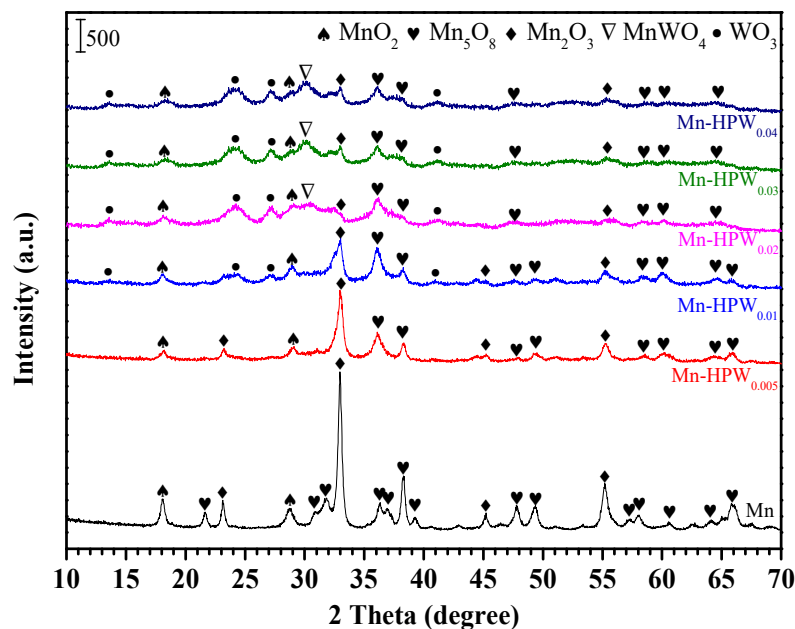


Figure 1. XRD patterns of Mn and Mn-HPW_x.

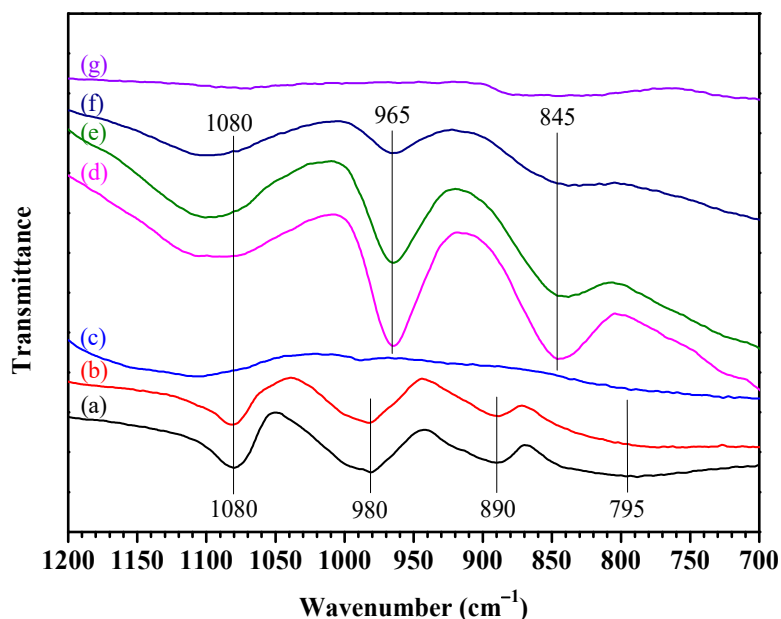


Figure 2. FTIR spectra of HPW before calcination (a), HPW calcinated at 400 °C (b) and 650 °C (c); Mn-HPW_{0.02} before calcination (d), Mn-HPW_{0.02} calcinated at 200 °C (e), 400 °C (f), and 650 °C (g).

2.1.3. N₂ Adsorption-Desorption

The textural properties of Mn, Mn-HPW_x, and HPW are summarized in Table 1. The specific BET surface areas (S_{BET}) of HPW and the Mn catalyst are 1.6 and 33.7 m²/g, respectively. The S_{BET} of Mn-HPW_x increases with x , reaching a maximum (69.1 m²/g) at $x = 0.02$, and then decreases when the x increases further. The value of the total pore volume increases only by 0.03–0.04 cm³/g as x is less than 0.02, while the total pore volume (0.14 cm³/g) is equal to the value of the Mn catalyst when $x = 0.02$ –0.04. These data reveal

that the influence of introducing HPW on the total pore volume over the Mn catalyst is negligible. For the average pore diameter over various samples, with the increase in the HPW content, the value first decreases and then increases after reaching the minimum on Mn-HPW_{0.02}, which is the opposite trend of the value of S_{BET} . N_2 adsorption/desorption isotherms are shown in Figure S4. All the catalysts exhibit a representative IV-type isotherm, accompanied by an obvious H3-type hysteric loop. The adsorption curve presents an upward tendency as the p/p_0 is higher than 0.6, revealing the existence of mesopores in all investigated catalysts. The ascending trend of the curves is obvious with p/p_0 higher than 0.8, meaning the presence of the macropores [56,57]. In the p/p_0 range of 0.6–0.8, the N_2 adsorption capacities on Mn-HPW_x ($x = 0.005$ – 0.02) are larger than those on Mn, and the hysteric loop is clearer, suggesting that the formation of more mesopores is facilitated by adding HPW, thus, increasing the values of S_{BET} and decreasing the average pore diameter. As the amount of HPW is higher than 0.02, the N_2 adsorption capacities with the p/p_0 higher than 0.8 are enhanced, demonstrating the formation of more macropores, thus, enlarging the average pore diameter.

Table 1. Surface area and pore structural characterizations of the Mn, Mn-HPW_x, and HPW catalysts.

Samples	BET Surface Area (m ² /g)	Total Pore Volume (cm ³ /g)	Average Pore Diameter (nm)
Mn	33.7	0.14	17.0
Mn-HPW _{0.005}	54.9	0.18	13.7
Mn-HPW _{0.01}	58.5	0.17	11.6
Mn-HPW _{0.02}	69.1	0.14	8.3
Mn-HPW _{0.03}	55.7	0.14	10.1
Mn-HPW _{0.04}	52.5	0.14	12.4
HPW	1.6	0.00	2.0

2.1.4. Morphology Structure

The SEM images of HPW, Mn, and Mn-HPW are exhibited in Figure 3. HPW presents a large bulk (Figure 3e), thus, leading to the small value of S_{BET} (coinciding with the results of Table 1). The rough, irregular, and agglomerated spherical particles can be observed on Mn (Figure 3b) and Mn-HPW_{0.02} (Figure 3c). Additionally, for Mn-HPW_{0.02}, the combination of HPW and $\text{Mn}(\text{NO}_3)_2$ can restrain the thermal growth of MnO_x and HPW during the calcination process, inducing the lower crystallinity of MnO_x and HPW (evidenced by the results of XRD), the smaller particles in Figure 3c, and the larger value of S_{BET} . The EDX elemental mapping of the Mn catalyst in Figure S5a–c displays that the Mn and O elements distribute well. The same situation is also obtained on Mn-HPW_{0.02}, in which W and P atoms are well dispersed (Figure S5d–h). TEM images of HPW, Mn, and Mn-HPW_{0.02} are shown in Figure 4. The clear lattice fringes ($d = 0.35$ nm) of HPW can be observed on the HPW catalyst (Figure 4b). The lattice fringes of Mn_2O_3 and Mn_5O_8 are shown on the Mn catalyst (Figure 4d). For Mn-HPW_{0.02} in Figure 4f,h, the lattice fringes of WO_3 and MnWO_4 are detected, and these are in accordance with the results of XRD.

2.2. Catalytic Performance

Initially, the effect of phosphomolybdic acid (HPMo), tungstosilicic acid (HSiW), and silicomolybdic acid (HSiMo), on the catalytic performance of the Mn catalyst for the NH_3 -SCR reaction was evaluated at 60–300 °C (Figure S6), and the molar ratio of Mn to heteropoly acid was set as 1 to 0.02. Among all investigated catalysts, Mn-HPW exhibits the broadest temperature window with 90–270 °C (>90% NO_x conversion). Therefore, the Mn-HPW catalyst is chosen for further investigation in this study.

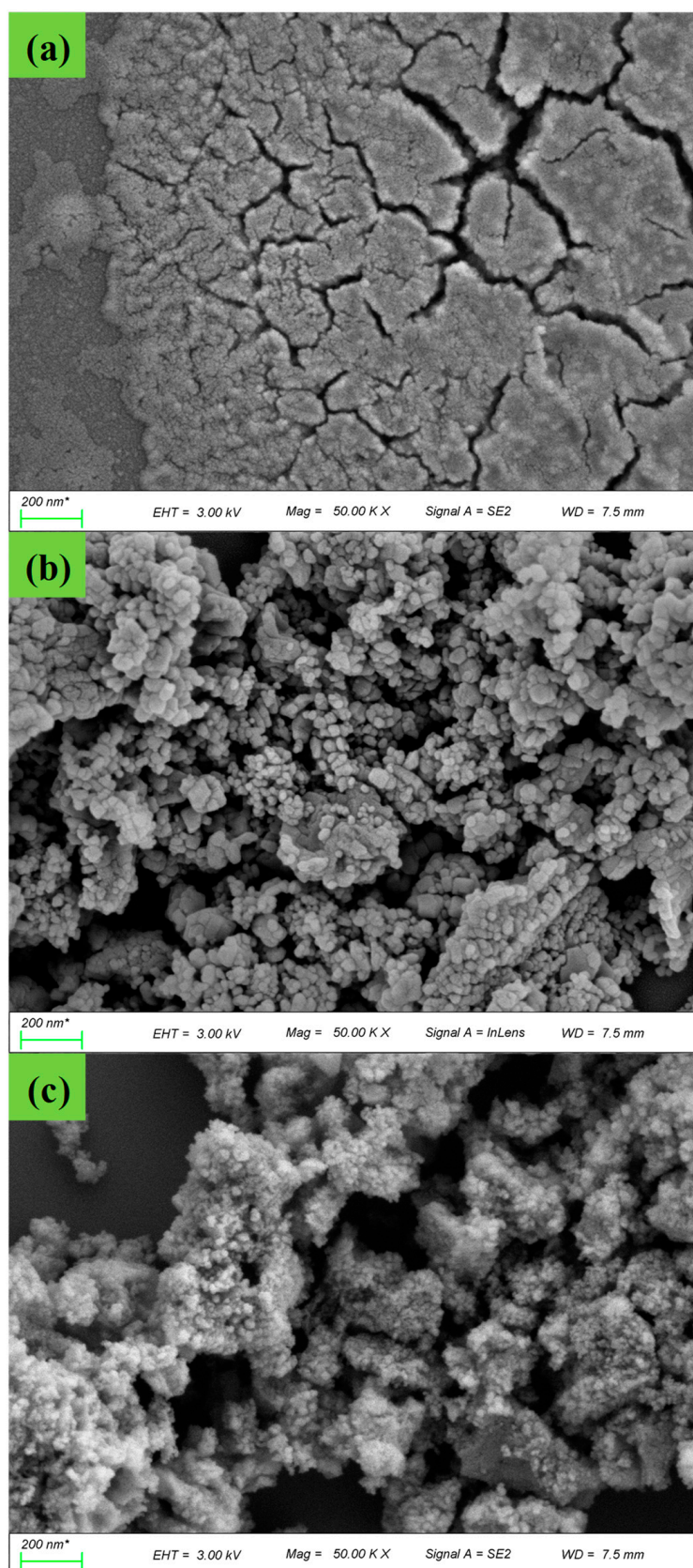


Figure 3. SEM images of HPW (a), Mn (b), and Mn-HPW_{0.02} (c).

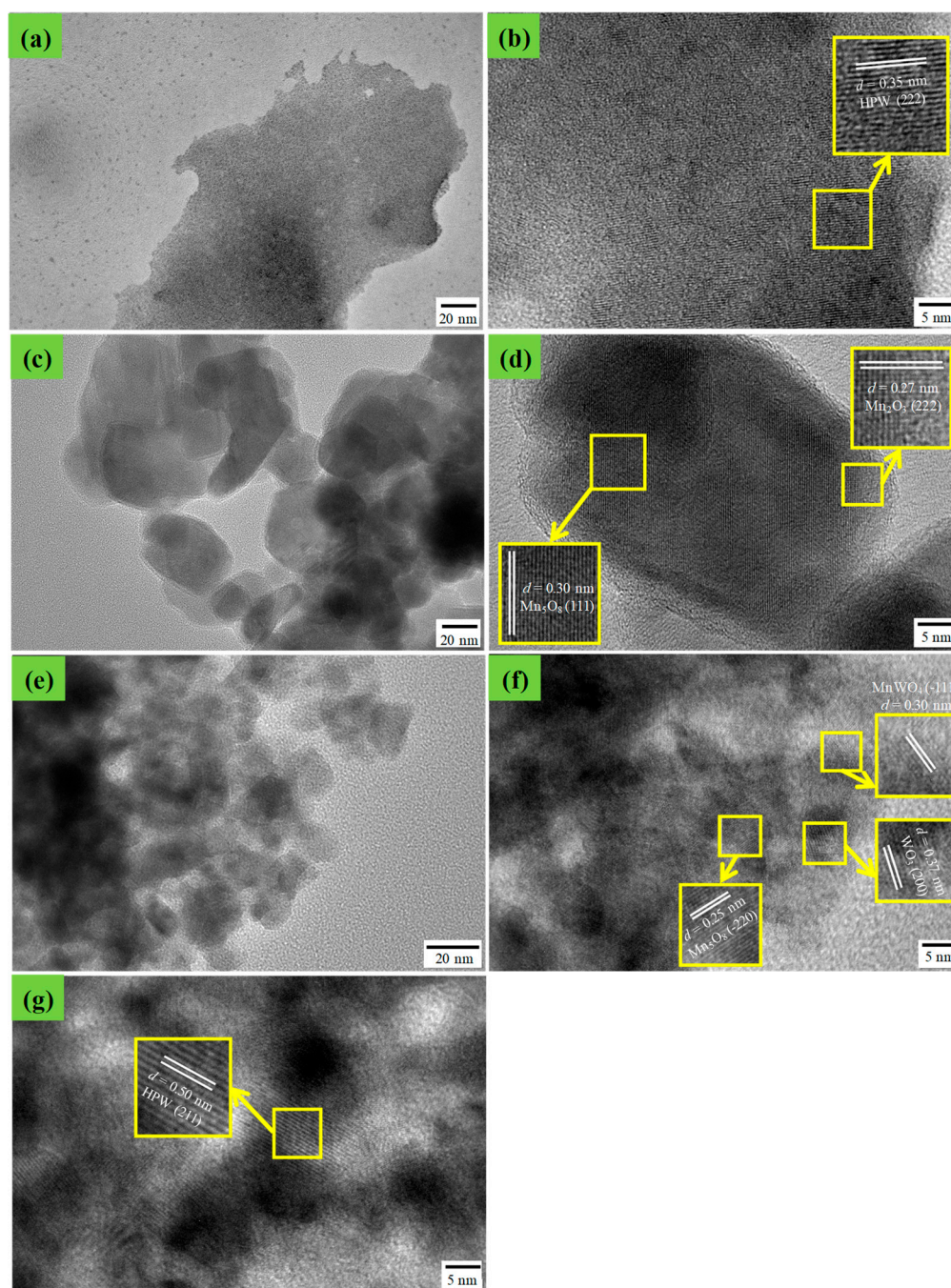


Figure 4. TEM images of HPW (a,b), Mn (c,d), and Mn-HPW_{0.02} (e–g).

Figure 5 shows the de-NO_x activities of Mn-HPW_x catalysts with a variety of molar ratios of HPW to Mn. HPW exhibits ~15% de-NO_x activity at 60–300 °C in Figure 5a. Mn shows higher activity at 60–300 °C, and 98% NO_x can be converted at 150 °C. The SCR activities on Mn-HPW_x catalysts are improved. For instance, at 60–180 °C (Figure 5b), the NO_x conversion enhances monotonously as the HPW/Mn molar ratio increases from 0.005 to 0.02 and then drops as the HPW/Mn molar ratio increases further. The maximum SCR activity can be obtained on Mn-HPW_{0.02}, in which case 96% NO_x conversion can be achieved at 90–180 °C. At 180–300 °C (Figure 5a), the activities on Mn-HPW_x are much higher than those on Mn, and the amount of doping HPW has a negligible effect on NO_x conversion. Based on the above results, Mn-HPW_{0.02} exhibits optimal de-NO_x activities. Additionally, Mn-HPW_{0.02} exhibits higher N₂ selectivity (Figure S7) and better SO₂ resistance (Figure S8).

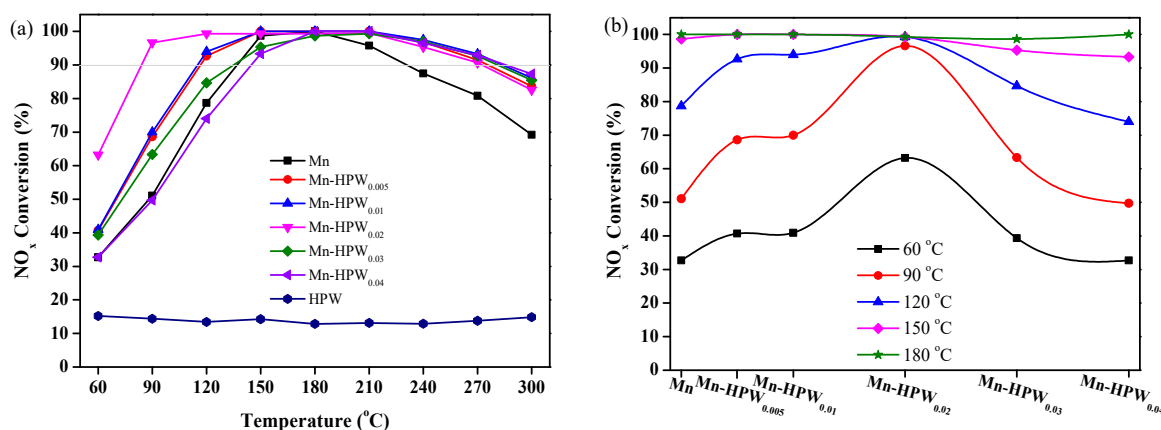


Figure 5. NH₃-SCR activity on HPW, Mn, and Mn-HPW_x at 60–300 °C (a) and at 60–180 °C (b).

The de-NO_x activity over the Mn catalyst can be enhanced by the modification with metal oxides, such as NbO_x [58], CoO_x [30], SmO_x [53], FeO_x [28], EuO_x [59], CuO_x [60], NiO_x [61], and CeO_x [62,63]. Table S1 lists some representative Mn-based catalysts for NH₃-SCR. For instance, more than 90% NO_x can be converted at 125–350 °C on Mn_xCo_{3-x}O₄ nanocages under relatively milder conditions (0.40 g catalyst, (NO) = 500 ppm, flow rate = 210 mL/min) [30]. Above 90% NO_x at 125–225 °C can be achieved on (Cu_{1.0}Mn_{2.0})_{1-δ}O₄ under conditions (0.15 g catalyst, (NO) = 500 ppm, flow rate = 200 mL/min) [60] similar to the conditions in our work. For comparison, Mn-HPW_{0.02} in our work showed > 90% NO_x conversion at 90–270 °C (0.15 g catalyst, (NO) = 500 ppm, flow rate = 200 mL/min). Hence, this catalyst was selected for further research.

2.3. NO and NH₃ Oxidation

The oxidation of NO to NO₂ is considered to be an essential reaction in the fast SCR reaction ($2\text{NH}_3 + \text{NO} + \text{NO}_2 \rightarrow 2\text{N}_2 + 3\text{H}_2\text{O}$). Thereby, catalytic NO oxidation over the Mn and Mn-HPW_{0.02} catalysts was performed (Figure 6a). The Mn catalyst presents a relatively high conversion of NO to NO₂ at 60–300 °C, while NO oxidation can be suppressed on Mn-HPW_{0.02}, illustrating the oxidation capacity is impaired on the Mn catalyst by doping HPW. Although the conversion for NO oxidation on Mn-HPW_{0.02} is lower than that on Mn, the NO_x conversion on Mn-HPW_{0.02} is much higher than that on Mn at low temperatures (Figure 5a), demonstrating that the improvement of the de-NO_x activity is not closely connected with fast SCR reaction over Mn-HPW_{0.02} in the low-temperature region, and similar situations associated with Mn-Nb [58] and Co-Ce-Mn-Ti catalysts [64] were also reported.

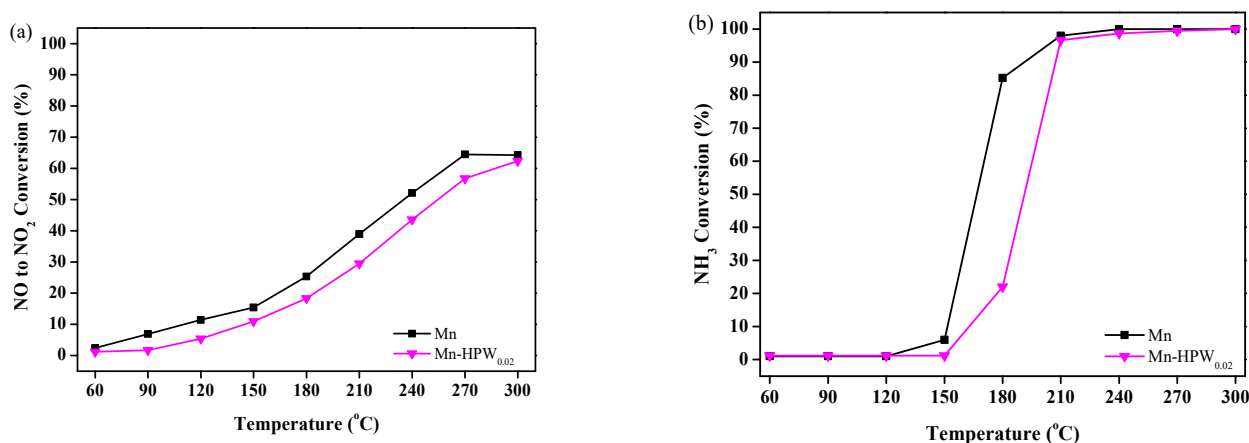


Figure 6. Conversion of NO to NO₂ (a) and NH₃ conversion (b) on Mn and Mn-HPW_{0.02} at 60–300 °C.

The decrease in NH₃-SCR activities at high temperatures has to do with the oxidation of NH₃. Thus, catalytic NH₃ oxidation on Mn and Mn-HPW_{0.02} at 60–300 °C was studied (Figure 6b). NH₃ oxidation can be ignored below 150 °C, and no by-products, such as N₂O, NO, and NO₂, can be detected in Figure S7. As the temperature is more than 150 °C, NH₃ conversion on both catalysts increases rapidly and reaches ~98% at 210 °C (Figure 6b). The yield of the by-products on Mn-HPW_{0.02} is much less than those on Mn at 180–270 °C in Figure S9. Obviously, the introduction of HPW can undermine the unselective oxidation of NH₃, promoting the conversion of NH₃ to N₂ ($4\text{NH}_3 + 3\text{O}_2 \rightarrow 2\text{N}_2 + 6\text{H}_2\text{O}$), and improving the N₂ selectivity.

2.4. H₂-TPR

The H₂-TPR data of the Mn, Mn-HPW_x, and HPW catalysts are shown in Figure 7. For HPW calcinated at 400 °C, no significant reduction peak of the tungsten species can be observed at 100–650 °C, because the decomposition temperature of HPW to WO₃ is 597 °C and the reduction temperature of WO₃ species is 828 °C [43,46]. The Mn catalyst shows two major reduction peaks at 150–360 °C (peak I) and 360–550 °C (peak II). Peak I is linked to the reduction of MnO₂ to Mn₂O₃, whereas peak II is involved in the reduction of Mn₂O₃ to Mn₃O₄ and Mn₃O₄ to MnO [25,50,65,66]. The reduction behavior changes, evidently, with the introduction of HPW as shown in Table S2. As the doping amount of HPW is increased, the areas of two reduction peaks decrease (Table S2). Meanwhile, the reduction temperature of the peak II peak shifts towards the higher temperature due to the suppression of electronic transmission between gaseous H₂ and MnO_x after adding HPW, and Geng et al. reported a similar situation [43]. It can be concluded that the addition of HPW weakens the reducibility of the MnO_x, consistent with the results of NO oxidation (Figure 4a) and NH₃ oxidation (Figure 4b). The moderate reducibility can suppress NH₃ unselective catalytic oxidization, thus, enhancing the conversion of NO_x and lessening the formation of by-product N₂O for NH₃-SCR [44,50,58]. In this case, Mn-HPW_{0.02} with moderate reducibility shows the optimal conversion of NO_x and the higher N₂ selectivity in SCR.

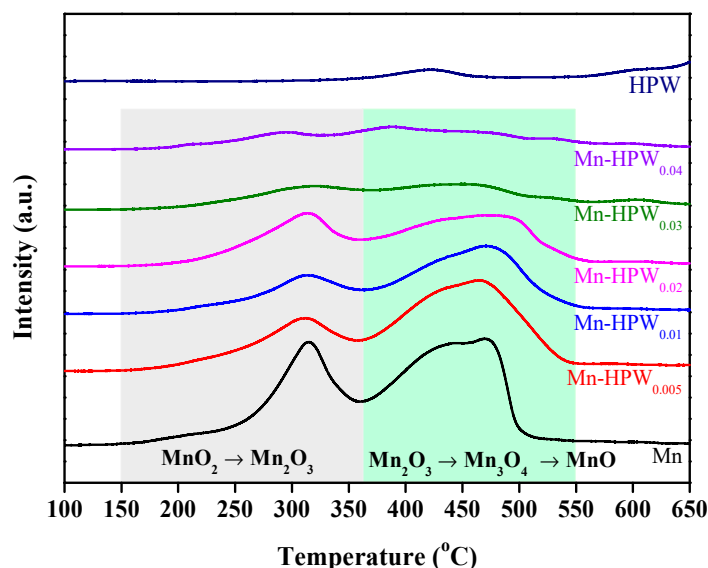


Figure 7. H₂-TPR profiles of Mn, Mn-HPW_x, and HPW.

2.5. XPS

XPS spectra of Mn 2p, W 4f, P 2p, and O 1s on Mn and Mn-HPW_x are illustrated in Figure 8. In Figure 8a, the peaks of Mn 2p_{3/2} and Mn 2p_{1/2} are inspected at ~642.0 eV and ~654.0 eV, respectively, and the Mn 2p_{3/2} spectra are deconvoluted and fitted by Gaussian-Lorentz into three subpeaks, including Mn²⁺ (640.8 ± 0.1 eV), Mn³⁺ (642.0 ± 0.2 eV),

and Mn^{4+} (643.5 ± 0.1 eV) [63,67,68]. The W 4f spectra on Mn-HPW_x in Figure 8b can be divided into two W^{6+} peaks at 35.3 ± 0.1 eV ($\text{W } 4f_{7/2}$) and 37.4 ± 0.1 eV ($\text{W } 4f_{5/2}$), respectively [44,69,70]. A broad peak at 133.5 ± 0.1 eV is attributed to P^{5+} in the P 2p spectra (Figure 8c) [54,71]. The surface atomic concentration of Mn element over Mn-HPW_x decreases with the increase in the content of HPW in Table 2, while the W and P concentrations enrich significantly. It is recognized that the Mn species with different valence states can influence the electron transfer and redox characteristics of the catalysts. For instance, Mn^{4+} and Mn^{3+} species are considered the active sites to adsorb and activate the reactants during NH_3 -SCR, and these species exhibit excellent redox properties, playing a vital role in the redox reaction ($\text{Mn}^{3+} \leftrightarrow \text{Mn}^{4+}$ and $\text{Mn}^{3+} \leftrightarrow \text{Mn}^{2+}$) [52,66]. The relative concentrations of Mn^{4+} and Mn^{3+} on Mn and Mn-HPW_x are listed in Table 2 and they decline gradually with the increase in HPW content owing to the electron transfer between W^{6+} in HPW and $\text{Mn}^{4+}/\text{Mn}^{3+}$ [36,50]. Since the high valence Mn species tend to facilitate the deep dehydrogenation of the adsorbed NH_3 species [50], the moderate decrease in the concentrations of Mn^{4+} species appropriately weakens the redox ability of MnO_x after adding HPW (identical to the results of H_2 -TPR, Figure 7), and then alleviates the over-oxidation of NH_3 (Figure 6b) and increases the N_2 selectivity [72].

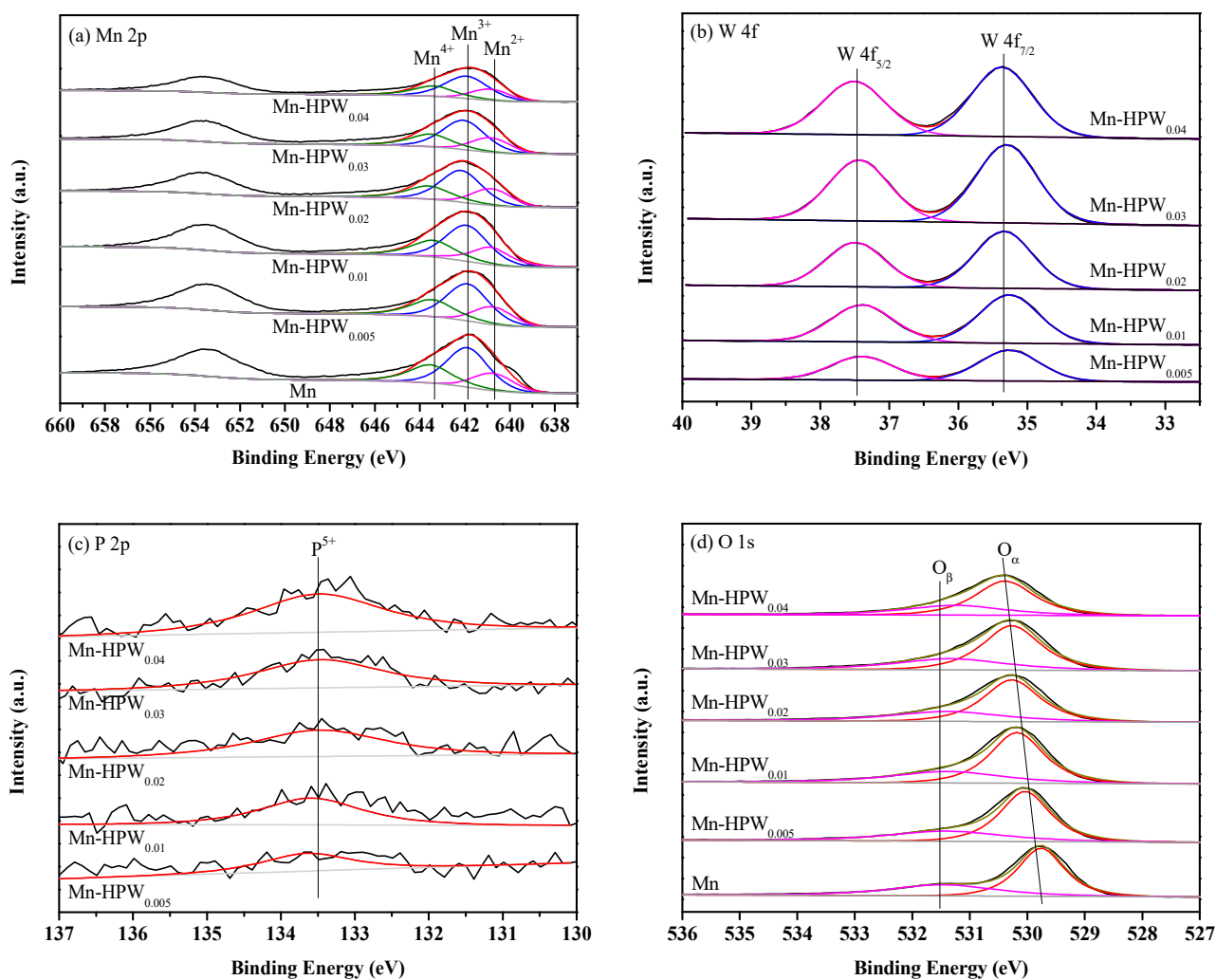


Figure 8. XPS results of Mn 2p (a), W 4f (b), P 2p (c), and O 1s (d) over Mn and Mn-HPW_x samples.

Table 2. Atomic surface concentrations on Mn and Mn-HPW_x.

Catalyst	Surface Atomic Concentration ¹ (at. %)				Relative Ratio ² (%)				Relative Concentration ³ (at. %)			
	Mn	O	W	P	Mn ⁴⁺ /Mn	Mn ³⁺ /Mn	Mn ²⁺ /Mn	O _β /O	Mn ⁴⁺	Mn ³⁺	Mn ²⁺	O _β
Mn	30.7	51.2	-	-	26.7	52.2	21.1	35.1	8.2	16.0	6.5	18.0
Mn-HPW _{0.005}	27.4	52.8	2.0	1.2	26.6	51.8	21.6	32.2	7.3	14.2	5.9	17.0
Mn-HPW _{0.01}	26.1	54.1	3.1	1.4	25.9	51.5	22.6	32.3	6.8	13.4	5.9	17.5
Mn-HPW _{0.02}	24.6	54.0	4.0	1.7	24.6	52.3	23.1	32.3	6.1	12.8	5.7	17.5
Mn-HPW _{0.03}	21.6	54.5	5.3	2.1	24.3	53.1	22.6	32.3	5.3	11.4	4.9	17.6
Mn-HPW _{0.04}	21.2	55.2	6.1	2.3	24.2	53.4	22.4	32.3	5.1	11.3	4.8	17.8

¹ The ratio of the Mn (or O, or W) atom to the sum of the measured elements (such as Mn, O, C, N, W, and P).

² The ratio of the corresponding peak areas in the XPS spectrum. ³ The relative concentration was calculated using the relative ratio multiplied by the surface atomic concentration.

Figure 8d displays the O 1s spectra of Mn-HPW_x. All curves involve two main peaks at 530.1 ± 0.3 eV (lattice oxygen (O_α)) and 531.3 ± 0.2 eV (surface chemisorbed oxygen (O_β)) [72–74]. The binding energy of O_α (529.8 eV) on the Mn catalyst moves to higher energy (530.4 eV) with the increase in the amount of HPW. This is related to the fact that HPW is composed of bridging metal atoms and oxygen atoms, and the lattice oxygen atoms in HPW are different from those in MnO_x [50,54]. From Table 2, increasing the HPW amount allows the oxygen atomic concentrations to enhance, whereas the relative concentrations of O_β with high mobility fluctuate slightly in the range of 17–18%, disclosing that the O_β concentration is not a main factor of controlling the de-NO_x activity.

2.6. NH₃ Adsorption

NH₃-TPD profiles of Mn and Mn-HPW_x are shown in Figure S10. Two desorption stages can be observed for all catalysts at 100–250 °C and 300–500 °C, corresponding to the desorption of NH₃ adsorbed on the weak acid sites and on the medium-strong acid sites, respectively [12,75]. After the Mn catalyst is doped with HPW, changes in the peak areas and the peak temperatures of NH₃ desorption are not obvious, illustrating that the effect of doping HPW on the acid number and acid strength is not obvious.

DRIFT spectra were recorded to further investigate the intermediates formed by adsorbed NH₃. The spectra of the NH₃-derived species on the Mn and Mn-HPW_{0.02} catalysts were collected at 60–300 °C (Figure 9). A couple of adsorbed NH₃ species form on the Mn surface after exposing NH₃ for 60 min (Figure 9a). The bands at 1220, 1290, and 1600 cm⁻¹ are attributed to the coordinated NH₃ bonded to the Lewis acid sites (L acid sites) [30,63,76], and the bands at 1445 and 1680 cm⁻¹ are assigned to the NH₄⁺ species adsorbed at the Brønsted acid sites (B acid sites) [12,19,30,72,76]. The bands of 1220, 1290, and 1600 cm⁻¹ on L acids sites and the bands of 1445 and 1680 cm⁻¹ display higher intensities at the low temperature, whereas these band intensities decrease gradually with rising desorption temperature. The band at 1330 cm⁻¹ appears at 300 °C, and it is ascribed to the partial oxidation/deformation of adsorbed ammonia species by the active surface oxygen species [15,27,74]. The bands at 1220, 1445, 1600, and 1680 cm⁻¹ are also detected on Mn-HPW_{0.02} in Figure 9b, and the variation trends of band intensities are close to those on Mn from 60 to 300 °C. Especially, the ammonia over Mn-HPW_{0.02} is adsorbed on L acid sites (1220 cm⁻¹), while the prevailing ammonia species over Mn is NH₄⁺ on B acid sites (1445 cm⁻¹), demonstrating that the introduction of HPW can promote the adsorption of more ammonia species on L acid sites. Moreover, no oxidation band (1330 cm⁻¹) of the adsorption NH₃ species can be detected at 300 °C. These phenomena illustrate that the oxidation ability of the Mn catalyst is weakened via adding an appropriate amount of HPW, thus protecting the adsorbed ammonia species from oxidation, in accordance with the results of the NH₃ oxidation activities (Figure 6b). The results mean that more ammonia species participate in the reaction with NO_x and increase the conversion of NO_x.

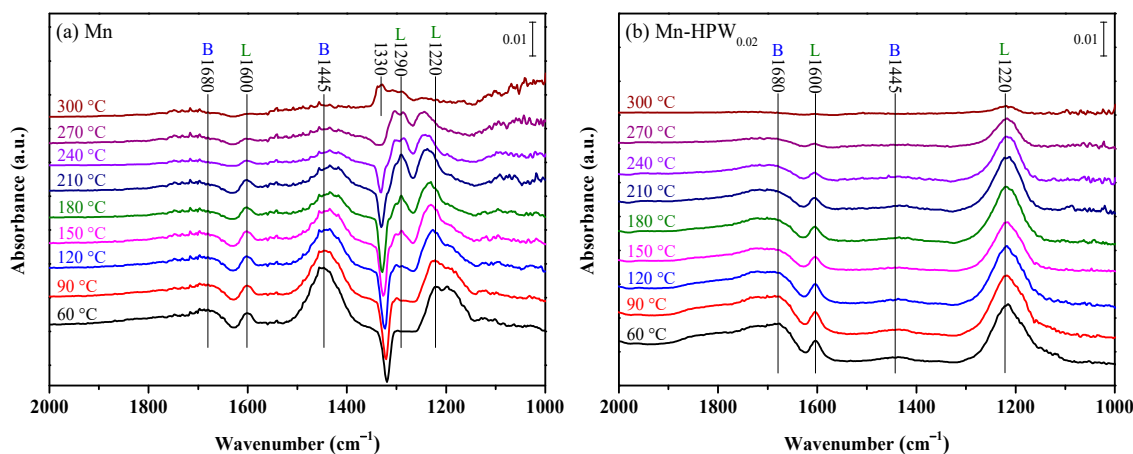


Figure 9. DRIFT spectra of NH₃-derived species on Mn (a), Mn-HPW_{0.02} (b) obtained by subtracting the corresponding background spectra. The catalysts were pretreated with 500 ppm NH₃ for 60 min and then purging by N₂ for 30 min at 30 °C.

2.7. NO_x Adsorption

Figure 10 exhibits the NO-TPD curves of the Mn, Mn-HPW_{0.005}, Mn-HPW_{0.02}, and Mn-HPW_{0.04} catalysts. The NO desorption can be divided into two regions at 50–500 °C. The peak at 50–200 °C is ascribed to the desorption of physically adsorbed NO and the decomposition of monodentate nitrite/nitrate species, while that at 200–500 °C is ascribed to the decomposition of bridged and bidentate nitrate species [77–79]. The amount of desorbed NO was calculated according to the NO-TPD curves. In contrast to the Mn catalyst (the desorption area of NO on Mn is set as 1.00), the peak areas of desorbed NO over Mn-HPW_x increase evidently, flowing the sequence of Mn-HPW_{0.02} (1.96) > Mn-HPW_{0.005} (1.68) > Mn-HPW_{0.04} (1.48) > Mn (1.00), meaning that the introduction of HPW enhances the NO adsorption capacity.

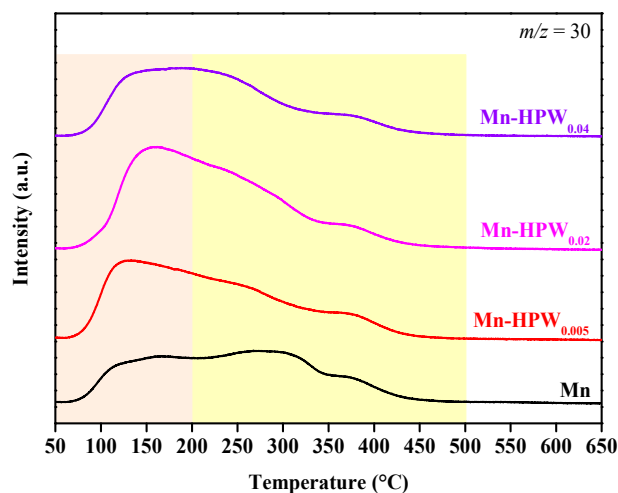


Figure 10. NO-TPD profiles on Mn, Mn-HPW_{0.005}, Mn-HPW_{0.02}, and Mn-HPW_{0.04}.

The intermediates of adsorbed NO_x complexes were studied with in situ DRIFT (Figure 11). After NO and O₂ were added to IR cell, the NO_x-derived species on Mn in Figure 11a appeared mainly at 1290, 1343, 1540, and 1627 cm⁻¹, and they can be attributed to monodentate nitrate (1290 cm⁻¹) [11,72,80], monodentate nitrite (1343 cm⁻¹) [27,73,81,82], bidentate nitrate (1540 cm⁻¹) [19,53,83–85], and bridged nitrate (1627 cm⁻¹) [19,36,53,86], respectively. The intensities of the adsorbed NO_x-derived species become weaker and weaker due to the decomposition of the nitrate and/or nitrite species as the temperature increases. The bands at 1290 and 1343 cm⁻¹ are hardly detected at 210 °C, demonstrating that

these species are weakly adsorbed. With respect to Mn-HPW_{0.02}, the bands at 1270 cm⁻¹ (monodentate nitrate), 1540 cm⁻¹, and 1627 cm⁻¹ are also observed in Figure 11b. As shown in Figure 11, bidentate nitrate (1540 cm⁻¹) is the leading species on Mn, while monodentate nitrate (1270 cm⁻¹) is dominant on Mn-HPW_{0.02}. Moreover, the bands of monodentate nitrate (1270 cm⁻¹) with the greater intensity on Mn-HPW_{0.02} are still clearly visible at 300 °C. The observation means that the introduction of HPW affects both the existence mode and stability of the nitrates.

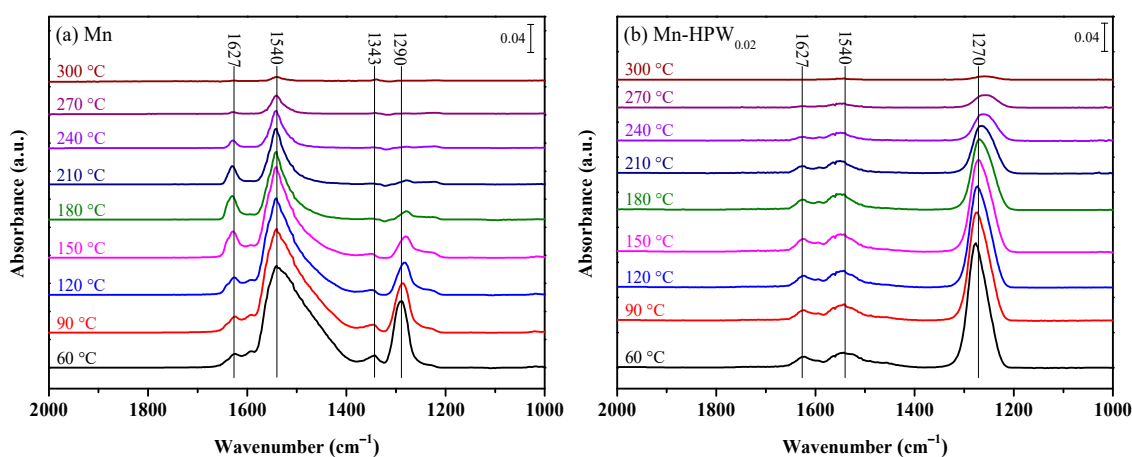


Figure 11. DRIFT spectra of NO_x-derived species on Mn (a) and Mn-HPW_{0.02} (b) obtained by subtracting the corresponding background spectra. The catalysts were pretreated with 500 ppm NO + 5% O₂ for 60 min and then purging by N₂ for 30 min at 30 °C.

2.8. Reaction Mechanism

2.8.1. Reaction between NO + O₂ and Pre-Adsorbed NH₃

At 120 °C, DRIFT spectra were acquired to reveal the reactivity of adsorbed ammonia species with NO + O₂. Coordinated NH₃ (1227 and 1600 cm⁻¹) and NH₄⁺ (1445 cm⁻¹) exist on the surface after Mn was pre-treated in NH₃ for 60 min in Figure 12a. With the mixture gas of NO and O₂ passing into IR cell, the band intensities of the adsorbed NH₃ species decrease gradually within 40 min and do not vanish completely (Figure S11a). This observation reveals that the reaction between the NH₃ species on L and B acid sites and gaseous NO_x follows the Eley–Rideal (E-R) route [87]. Especially, the band intensity of NH₄⁺ at 1445 cm⁻¹ barely changes in the first 10 min after the introduction of NO + O₂, and then increases slightly within 20 min due to the formation of NH₄NO₂ [88]. After the exposure to the mixture of NO and O₂ is longer than 40 min, the adsorbed NO_x-derived species, i.e., monodentate nitrate (1255 cm⁻¹), bidentate nitrate (1530 cm⁻¹), and bridged nitrate (1627 cm⁻¹) emerge on Mn surface, and the bands of these species partially overlap with those of the unreacted NH₃ species. For instance, the emergence of bidentate nitrate at 1530 cm⁻¹ influences the intensity of NH₄⁺ at 1445 cm⁻¹. The spectra on Mn-HPW_{0.02} are demonstrated in Figure 12b. The bands of NH₃ species on L acid sites (1220 and 1600 cm⁻¹) and B acid sites (1680 cm⁻¹) diminish quickly and then disappear as NO and O₂ were employed for 30 min in Figure S11b. Subsequently, the bands of monodentate nitrate (1270 cm⁻¹) and bridged nitrate (1627 cm⁻¹) become apparent. In Figure S11a,b, NH₃ species on Mn and Mn-HPW_{0.02} begin to be consumed as the NO and O₂ are passed for 20 min and 5 min, respectively, indicating that HPW can enhance the reactivity of ammonia species. Additionally, the intensity of NH₃ species on L acid sites (1220/1227 cm⁻¹) decreases faster than that on B acid sites, illustrating that NH₃ species on L acid sites possess higher reactivity. For the NH₃ pre-adsorbed catalysts, Mn-HPW_{0.02} shows a more coordinated NH₃ species than Mn. Therefore, Mn-HPW_{0.02} exhibits excellent SCR activity in the low-temperature region, which coincides with the results in Figure 5a.

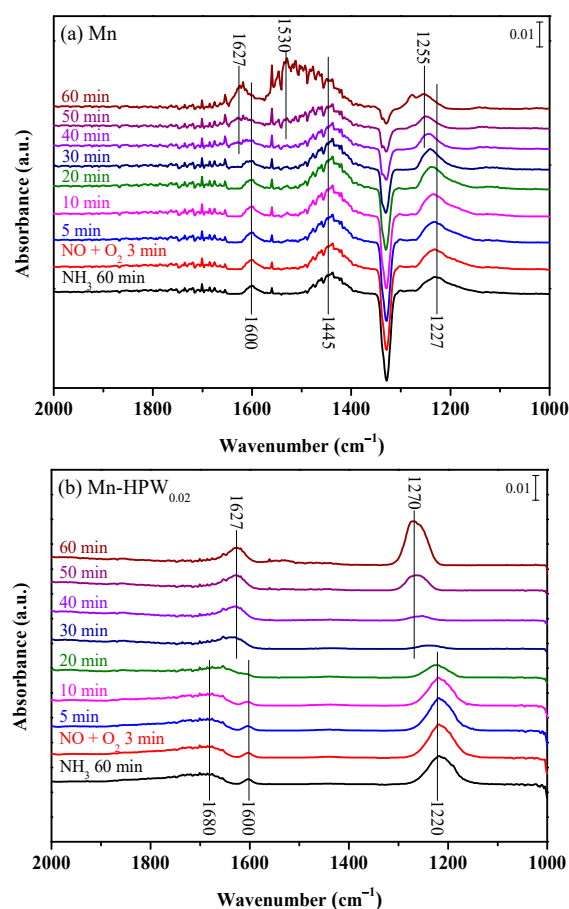


Figure 12. DRIFT spectra obtained by subtracting the corresponding background spectra of NO + O₂ reacted with pre-adsorbed NH₃ species at 120 °C on Mn (a) and Mn-HPW_{0.02} (b).

2.8.2. Reaction between NH₃ and Pre-Adsorbed NO + O₂

The reaction DRIFT spectra of the pre-adsorbed NO + O₂ species with NH₃ at 120 °C on Mn and Mn-HPW_{0.02} are presented in Figure 13. The bands of the monodentate nitrate (1280 cm⁻¹), bidentate nitrate (1540 cm⁻¹), and bridged nitrate (1630 cm⁻¹) form on the Mn surface after pretreated in NO and O₂ for 60 min in Figure 13a. The dependence of the intensities of the NO_x-derived species on exposure time to NH₃ is also shown in Figure S12a. As the introduction time of NH₃ is less than 10 min, the change of band at 1280 cm⁻¹ is ignorable, while the band intensities at 1540 and 1630 cm⁻¹ attenuate progressively, and the band at 1630 cm⁻¹ vanishes after exposing to NH₃ for 20 min. These demonstrate that monodentate nitrate (1280 cm⁻¹) is inactive in NH₃-SCR, whereas the reaction of bidentate nitrate (1540 cm⁻¹) and/or bridged nitrate (1630 cm⁻¹) with adsorbed ammonia species obey the Langmuir–Hinshelwood (L-H) pathway [74,82,87]. As the NH₃ continues to enter the system, the bands adsorbed on L acid sites (1240, 1290, and 1600 cm⁻¹), B acid sites (1445 cm⁻¹), and the oxidation/deformation of adsorbed ammonia species (1350 cm⁻¹) become visible on the Mn surface. Additionally, the bands of adsorbed NH₃ species at 1290 cm⁻¹ cover those of monodentate nitrate (1280 cm⁻¹), and the bands of NH₄⁺ at 1445 cm⁻¹ overlap with those of bidentate nitrate (1540 cm⁻¹). For the spectra of Mn-HPW_{0.02}, the NO_x-derived species containing monodentate nitrate (1270 cm⁻¹), bidentate nitrate (1550 cm⁻¹), and bridged nitrate (1630 cm⁻¹) are formed (Figure S12b and Figure 13b). With the introduction of NH₃, the variation tendencies of these band intensities are similar to those on Mn, confirming that the L-H mechanism is also appropriate for Mn-HPW_{0.02}. Notably, compared with the reaction rate of adsorbed NH₃ species with NO_x (Figure S11b), the reaction rate of adsorbed NO_x-derived species with NH₃ (Figure S12b) is slower. Furthermore, the introduction of HPW promotes the adsorption of more NH₃

species on L acid sites. Thus, the E-R mechanism on Mn-HPW_{0.02} plays a dominant role and further enhances the performance for NH₃-SCR reaction.

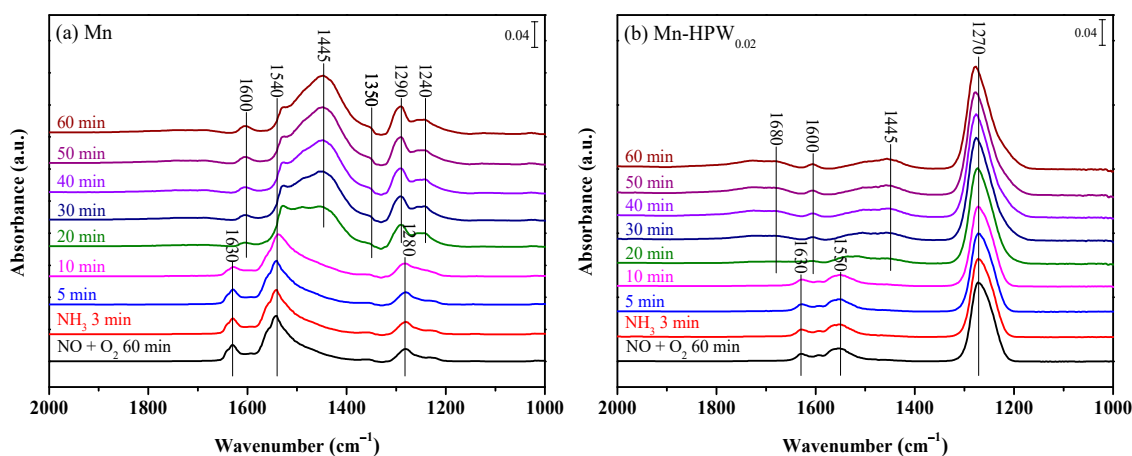


Figure 13. DRIFT spectra obtained by subtracting the corresponding background spectra of of NH₃ reacted with pre-adsorbed NO_x-derived species at 120 °C on Mn (a) and Mn-HPW_{0.02} (b).

3. Materials and Methods

3.1. Catalyst Preparation

H₃PW₁₂O₄₀-modified MnO_x catalysts were prepared as follows. First, 12.0 g aqueous Mn(NO₃)₂ solution (50%, Sinopharm, Shanghai, China), 4.2 g oxalic acid dihydrate (OA, ≥ 99.0%, Adamas, Shanghai, China), 2.1 g ethylene glycol (EG, ≥ 99.0%, Adamas), and the required amounts of tungstophosphoric acid (H₃PW₁₂O₄₀, HPW, 99%, Adamas) were added into an agate mortar. The sample was transferred into a beaker after hand grinding for 30 min, and subjected to ultrasonication for 30 min. The slurry was dried at 110 °C for 12 h, and then calcinated at 400 °C for 4 h to obtain Mn-HPW_x, in which x represents the HPW/Mn molar ratio (0.005–0.04) and the molar ratio of Mn:OA:EG is 1:1:1. Moreover, the mono-component Mn catalyst was also prepared with the same process without adding HPW. HPW was prepared as a reference with a molar ratio of OA:EG:HPW = 1:1:0.02.

3.2. Characterization

X-ray diffraction data were obtained by a Bruker D8 Advance instrument (Karlsruhe, Germany). Textural properties of catalysts were analyzed at −196 °C on a Micromeritics ASAP-2020 HD88 adsorption apparatus (Norcross, GA, USA). The morphologies and EDX mapping data of samples were gained on ZEISS Gemini 300 (Oberkochen, Germany). TEM images were observed with a JEM-2100plus TEM instrument (Tokyo, Japan).

Temperature-programmed reduction with hydrogen (H₂-TPR) and temperature-programmed desorption of NH₃ (NH₃-TPD) were performed by a thermal conductivity detector. First, a certain amount of catalyst was pretreated by N₂ at 300 °C for 30 min and then cooled down to 30 °C. In H₂-TPR experiment, 10% H₂/N₂ (50 mL/min) was introduced to 50 mg of catalyst, and then, the reduction experiments proceeded to 650 °C at 5 °C/min. For NH₃-TPD, 100 mg sample was saturated with 10% NH₃/N₂ for 30 min at 30 °C followed by being flushed with N₂ for 30 min at 100 °C, and subsequently, heated to 500 °C at 5 °C/min.

X-ray photoelectron spectroscopy (XPS) measurements were performed with an ESCALAB 250 Xi spectrometer (Thermo Fisher Scientific, Waltham, MA, USA).

Temperature-programmed desorption of NO (NO-TPD) was conducted on a mass spectrometer (Pfeiffer Vacuum Quadstar, 32-bit, Aßlar, Germany). First, 100 mg catalyst was pretreated in He (30 mL/min) at 300 °C for 30 min. Subsequently, the sample was flushed with 500 ppm NO/N₂ and 5 vol % O₂ for 1 h after cooling down to 30 °C. He gas was passed for 30 min at 50 °C, and then the NO-TPD test was started from 50 to 650 °C at 5 °C/min.

In-situ DRIFT data were obtained on a Nicolet 6700 spectrometer (Waltham, MA, USA) with 64 accumulated scans and a resolution of 4 cm^{-1} . The sample was treated at $300\text{ }^\circ\text{C}$ in N_2 flow for 30 min. Subsequently, the background spectra were collected at the corresponding temperatures under N_2 flow during the cooling process and were subtracted from each sample spectra in the test. For the experiments of NH_3 or NO_x adsorption at different temperatures, the catalysts were pretreated under the condition of 500 ppm NH_3 or 500 ppm $\text{NO} + 5\% \text{O}_2$ for 60 min at $30\text{ }^\circ\text{C}$, followed by purging with N_2 for 30 min. DRIFT spectra of adsorbed NH_3 - or NO_x -derived species are collected at the corresponding temperature under the N_2 atmosphere. With regards to the experiments of transient reaction, the catalysts were pretreated with 500 ppm NH_3 or 500 ppm $\text{NO} + 5\% \text{O}_2$ at $120\text{ }^\circ\text{C}$ for 60 min, and the spectra were recorded at different times. Subsequently, the samples were purged by N_2 at $120\text{ }^\circ\text{C}$ for 30 min, and finally, the mixture gas of 500 ppm $\text{NO} + 5\% \text{O}_2$ + or 500 ppm NH_3 was introduced into the IR cell to react with the NH_3 - or NO_x -derived species, collecting the spectra at different times.

3.3. Catalytic Activity Test

The activities were evaluated in a fixed quartz reactor. The reaction gas was composed of 500 ppm NO , 500 ppm NH_3 , 5% O_2 , 50 ppm SO_2 (when used), and balanced N_2 . The gas flow rate was kept at 200 mL/min (WHSV = $80,000\text{ mL g}^{-1}\text{ h}^{-1}$). The concentration of NO and NO_2 in the reaction gas was determined with a flue gas analyzer (Testo 340, Lenzkirch, Germany) and the concentration of N_2O was obtained by a gas chromatograph (Panna A91, China). NO_x conversion and N_2 selectivity were calculated [52,89,90]:

$$\text{NO}_x \text{ conversion (\%)} = \frac{[\text{NO}_x]_{\text{inlet}} - [\text{NO}_x]_{\text{outlet}}}{[\text{NO}_x]_{\text{inlet}}} \times 100\% \quad (1)$$

$$\text{N}_2 \text{ selectivity} = \left(1 - \frac{2 \times [\text{N}_2\text{O}]_{\text{outlet}}}{[\text{NO}_x]_{\text{inlet}} + [\text{NH}_3]_{\text{inlet}}} \right) \times 100\% \quad (2)$$

The individual NO (NH_3) oxidation reaction was performed on the same devices without the introduction of NH_3 (NO). A detector (LY500- NH_3 - H_2) was employed to record the concentration of NH_3 in effluent gas, and NO and NH_3 oxidation conversion were calculated:

$$\text{NO conversion (\%)} = \frac{[\text{NO}]_{\text{inlet}} - [\text{NO}]_{\text{outlet}}}{[\text{NO}]_{\text{inlet}}} \times 100\% \quad (3)$$

$$\text{NH}_3 \text{ conversion (\%)} = \frac{[\text{NH}_3]_{\text{inlet}} - [\text{NH}_3]_{\text{outlet}}}{[\text{NH}_3]_{\text{inlet}}} \times 100\% \quad (4)$$

4. Conclusions

HPW-modified MnO_x catalysts were prepared for NO_x removal. The effect of the HPW doping amount on the activities over the Mn catalyst was evaluated. Additionally, the correlation between physicochemical properties and NH_3 -SCR performance, and reaction mechanisms were surveyed via several characterizations. The conclusions can be drawn.

(1) The Mn catalyst modified by HPW possesses good NH_3 -SCR activity and above 90% NO_x conversion at $90\text{--}270\text{ }^\circ\text{C}$ can be obtained on Mn-HPW_{0.02} along with relatively higher N_2 selectivity.

(2) The NH_3 species on Lewis and Brønsted acid sites can take part in NH_3 -SCR, and the reactivity of NH_3 species on Lewis acid sites is higher than those on Brønsted acid sites. The amount of Lewis acid sites increases obviously after adding HPW to the Mn catalyst, and the reaction of adsorbed NH_3 species with gas-phase NO_x is accelerated on Mn-HPW_{0.02}, thus, boosting low-temperature activities.

(3) The reduction temperatures of the MnO_x species move towards the higher temperature and the concentration of Mn^{4+} decreases, which weakens moderately the oxidation abilities of the Mn catalyst modified by HPW and protects the adsorbed NH_3 species from the overoxidation. Therefore, NO_x elimination and N_2 selectivity are improved at high temperatures.

(4) Among the NO_x -derived species, the bridged nitrate and bidentate nitrate on Mn and Mn-HPW_{0.02} have the higher reactivity, reacting with adsorbed NH_3 species, while monodentate nitrate species fail to do so. At 120 °C, both E-R and L-H routes are suitable for the Mn and Mn-HPW_{0.02} catalysts for NH_3 -SCR, and the E-R mechanism is dominant on Mn-HPW_{0.02}.

Supplementary Materials: The following supporting information can be downloaded at: <https://www.mdpi.com/article/10.3390/catal12101248/s1>, Figure S1: XRD patterns of the Mn samples and the standard patterns of MnO_2 , Mn_5O_8 , and Mn_2O_3 phases; Figure S2: XRD patterns of HPW calcinated at 400 °C and 650 °C; the standard patterns of HPW and WO_3 phases; Figure S3: XRD patterns of Mn-HPW_{0.02} before calcination, Mn-HPW_{0.02} calcinated at 200 °C, 400 °C, and 650 °C; the standard patterns of MnWO_4 phases; Figure S4: N_2 adsorption–desorption isotherms on the Mn and Mn-HPW_x catalysts; Figure S5: EDX mapping of Mn (a–c) and Mn-HPW_{0.02} (d–h); Figure S6: NH_3 -SCR activity on Mn, Mn-HPW, Mn-HPMo, Mn-HSiW, and Mn-HSiMo at 60–300 °C; Figure S7: N_2 selectivity on the Mn and Mn-HPW_{0.02} catalysts at 60–300 °C; Figure S8: Effect of 50 ppm SO_2 on NH_3 -SCR activity over the Mn and Mn-HPW_{0.02} catalysts at 150 °C; Figure S9: Yield of N_2O , NO , and NO_2 on Mn and Mn-HPW_{0.02} at 60–300 °C; Figure S10: NH_3 -TPD profiles of the Mn and Mn-HPW_x catalysts; Figure S11: Dependence of the band intensities of NH_3 -derived species on time over Mn (a) and Mn-HPW_{0.02} (b); Figure S12: Dependence of the band intensities of the NO_x -derived species on time over Mn (a) and Mn-HPW_{0.02} (b); Table S1: Representative Mn-based catalysts decorated by different assistant for NH_3 -SCR; Table S2: Reduction temperature and relative ratio in H_2 -TPR curves.

Author Contributions: Conceptualization, H.X. and X.G.; methodology, H.X.; validation, D.M., T.M. and J.Y.; formal analysis, H.X.; investigation, H.X. and X.G.; resources, D.M. and T.M.; data curation, H.X.; writing—original draft preparation, H.X.; writing—review and editing, H.X., X.G., D.M. and Z.M.; visualization, H.X.; supervision, X.G. and Z.M.; project administration, D.M.; funding acquisition, T.M. and Z.M. All authors have read and agreed to the published version of the manuscript.

Funding: This work was supported by Opening Project of Shanghai Key Laboratory of Atmospheric Particle Pollution and Prevention (LAP³) (FDLAP21007).

Data Availability Statement: Data are available from the authors.

Conflicts of Interest: The authors declare no conflict of interest.

References

1. Huang, R.J.; Zhang, Y.L.; Bozzetti, C.; Ho, K.F.; Cao, J.J.; Han, Y.M.; Daellenbach, K.R.; Slowik, J.G.; Platt, S.M.; Canonaco, F.; et al. High secondary aerosol contribution to particulate pollution during haze events in China. *Nature* **2014**, *514*, 218–222. [CrossRef]
2. Han, L.P.; Cai, S.X.; Gao, M.; Hasegawa, J.Y.; Wang, P.L.; Zhang, J.P.; Shi, L.Y.; Zhang, D.S. Selective catalytic reduction of NO_x with NH_3 by using novel catalysts: State of the art and future prospects. *Chem. Rev.* **2019**, *119*, 10916–10976. [CrossRef]
3. Xu, G.Y.; Guo, X.L.; Cheng, X.X.; Yu, J.; Fang, B.Z. A review of Mn-based catalysts for low-temperature NH_3 -SCR: NO_x removal and $\text{H}_2\text{O}/\text{SO}_2$ resistance. *Nanoscale* **2021**, *13*, 7052–7080. [CrossRef]
4. Wei, L.G.; Guo, R.T.; Zhou, J.; Qin, B.; Chen, X.; Bi, Z.X.; Pan, W.G. Chemical deactivation and resistance of Mn-based SCR catalysts for NO_x removal from stationary sources. *Fuel* **2022**, *316*, 123438. [CrossRef]
5. Guo, R.T.; Qin, B.; Wei, L.G.; Yin, T.Y.; Zhou, J.; Pan, W.G. Recent progress of low-temperature selective catalytic reduction of NO_x with NH_3 over manganese oxide-based catalysts. *Phys. Chem. Chem. Phys.* **2022**, *24*, 6363–6382. [CrossRef]
6. Zhang, L.; Zhang, D.S.; Zhang, J.P.; Cai, S.X.; Fang, C.; Huang, L.; Li, H.R.; Gao, R.H.; Shi, L.Y. Design of meso- $\text{TiO}_2@\text{MnO}_x\text{-CeO}_x/\text{CNTs}$ with a core-shell structure as DeNO_x catalysts: Promotion of activity, stability and SO_2 -tolerance. *Nanoscale* **2013**, *5*, 9821–9829. [CrossRef] [PubMed]
7. Zhang, S.G.; Zhang, B.L.; Liu, B.; Sun, S.L. A review of Mn-containing oxide catalysts for low temperature selective catalytic reduction of NO_x with NH_3 : Reaction mechanism and catalyst deactivation. *RSC Adv.* **2017**, *7*, 26226–26242. [CrossRef]
8. Huang, C.Y.; Guo, R.T.; Pan, W.G.; Sun, X.; Liu, S.W.; Liu, J.; Wang, Z.Y.; Shi, X. SCR of NO_x by NH_3 over $\text{MnFeO}_x@\text{TiO}_2$ catalyst with a core-shell structure: The improved K resistance. *J. Energy Inst.* **2019**, *92*, 1364–1378. [CrossRef]

9. Shi, Y.R.; Yi, H.H.; Gao, F.Y.; Zhao, S.Z.; Xie, Z.L.; Tang, X.L. Facile synthesis of hollow nanotube MnCoO_x catalyst with superior resistance to SO₂ and alkali metal poisons for NH₃-SCR removal of NO_x. *Sep. Purif. Technol.* **2021**, *265*, 118517. [[CrossRef](#)]
10. Liu, C.; Shi, J.-W.; Gao, C.; Niu, C.M. Manganese oxide-based catalysts for low-temperature selective catalytic reduction of NO_x with NH₃: A review. *Appl. Catal. A Gen.* **2016**, *522*, 54–69. [[CrossRef](#)]
11. Jiang, B.Q.; Lin, B.L.; Li, Z.G.; Zhao, S.; Chen, Z.Y. Mn/TiO₂ catalysts prepared by ultrasonic spray pyrolysis method for NO_x removal in low-temperature SCR reaction. *Colloids Surf. A Physicochem. Eng. Asp.* **2020**, *586*, 124210. [[CrossRef](#)]
12. Wei, L.; Wang, Z.W.; Liu, Y.; Guo, G.S.; Dai, H.X.; Cui, S.P.; Deng, J.G. Support promotion effect on the SO₂ and K⁺ co-poisoning resistance of MnO₂/TiO₂ for NH₃-SCR of NO. *J. Hazard. Mater.* **2021**, *416*, 126117. [[CrossRef](#)] [[PubMed](#)]
13. Kang, H.; Wu, M.X.; Li, S.Y.; Wei, C.H.; Chen, X.P.; Chen, J.J.; Jing, F.L.; Chu, W.; Liu, Y.F. Converting poisonous sulfate species to an active promoter on TiO₂ predecorated MnO_x catalysts for the NH₃-SCR reaction. *ACS Appl. Mater. Interfaces* **2021**, *13*, 61237–61247. [[CrossRef](#)]
14. Cao, F.; Xiang, J.; Su, S.; Wang, P.Y.; Sun, L.S.; Hu, S.; Lei, S.Y. The activity and characterization of MnO_x-CeO₂-ZrO₂/γ-Al₂O₃ catalysts for low temperature selective catalytic reduction of NO with NH₃. *Chem. Eng. J.* **2014**, *243*, 347–354. [[CrossRef](#)]
15. Cao, F.; Su, S.; Xiang, J.; Wang, P.Y.; Hu, S.; Sun, L.S.; Zhang, A.C. The activity and mechanism study of Fe-Mn-Ce/γ-Al₂O₃ catalyst for low temperature selective catalytic reduction of NO with NH₃. *Fuel* **2015**, *139*, 232–239. [[CrossRef](#)]
16. Yang, G.; Zhao, H.T.; Luo, X.; Shi, K.Q.; Zhao, H.B.; Wang, W.K.; Chen, Q.H.; Fan, H.; Wu, T. Promotion effect and mechanism of the addition of Mo on the enhanced low temperature SCR of NO_x by NH₃ over MnO_x/γ-Al₂O₃ catalysts. *Appl. Catal. B Environ.* **2019**, *245*, 743–752. [[CrossRef](#)]
17. Wang, L.S.; Huang, B.C.; Su, Y.X.; Zhou, G.Y.; Wang, K.L.; Luo, H.C.; Ye, D.Q. Manganese oxides supported on multi-walled carbon nanotubes for selective catalytic reduction of NO with NH₃: Catalytic activity and characterization. *Chem. Eng. J.* **2012**, *192*, 232–241. [[CrossRef](#)]
18. Zhou, Y.H.; Su, B.X.; Ren, S.; Chen, Z.C.; Su, Z.H.; Yang, J.; Chen, L.; Wang, M.M. Nb₂O₅-modified Mn-Ce/AC catalyst with high ZnCl₂ and SO₂ tolerance for low-temperature NH₃-SCR of NO. *J. Environ. Chem. Eng.* **2021**, *9*, 106323. [[CrossRef](#)]
19. Yang, J.; Ren, S.; Su, B.X.; Wang, M.M.; Chen, L.; Liu, Q.C. Understanding the dual-acting of iron and sulfur dioxide over Mn-Fe/AC catalysts for low-temperature SCR of NO. *Mol. Catal.* **2022**, *519*, 112150. [[CrossRef](#)]
20. Lou, X.R.; Liu, P.; Li, J.; Li, Z.; He, K. Effects of calcination temperature on Mn species and catalytic activities of Mn/ZSM-5 catalyst for selective catalytic reduction of NO with ammonia. *Appl. Surf. Sci.* **2014**, *307*, 382–387. [[CrossRef](#)]
21. Li, J.; Guo, J.X.; Shi, X.K.; Wen, X.R.; Chu, Y.H.; Yuan, S.D. Effect of aluminum on the catalytic performance and reaction mechanism of Mn/MCM-41 for NH₃-SCR reaction. *Appl. Surf. Sci.* **2020**, *534*, 147592. [[CrossRef](#)]
22. Lu, P.; Ye, L.; Yan, X.H.; Fang, P.; Chen, X.B.; Chen, D.S.; Cen, C.P. Impact of toluene poisoning on MnCe/HZSM-5 SCR catalyst. *Chem. Eng. J.* **2021**, *414*, 128838. [[CrossRef](#)]
23. Qi, G.; Yang, R.T.; Chang, R. MnO_x-CeO₂ mixed oxides prepared by co-precipitation for selective catalytic reduction of NO with NH₃ at low temperatures. *Appl. Catal. B Environ.* **2004**, *51*, 93–106. [[CrossRef](#)]
24. Liu, Z.M.; Yi, Y.; Zhang, S.X.; Zhu, T.L.; Zhu, J.Z.; Wang, J.G. Selective catalytic reduction of NO_x with NH₃ over Mn-Ce mixed oxide catalyst at low temperatures. *Catal. Today* **2013**, *216*, 76–81. [[CrossRef](#)]
25. Li, W.M.; Liu, H.D.; Chen, Y.F. Fabrication of MnO_x-CeO₂-based catalytic filters and their application in low-temperature selective catalytic reduction of NO with NH₃. *Ind. Eng. Chem. Res.* **2020**, *59*, 12657–12665. [[CrossRef](#)]
26. Fang, X.; Liu, Y.J.; Cheng, Y.; Chen, W.L. Mechanism of Ce-modified birnessite-MnO₂ in promoting SO₂ poisoning resistance for low-temperature NH₃-SCR. *ACS Catal.* **2021**, *11*, 4125–4135. [[CrossRef](#)]
27. Yang, S.J.; Wang, C.Z.; Li, J.H.; Yan, N.Q.; Ma, L.; Chang, H.Z. Low temperature selective catalytic reduction of NO with NH₃ over Mn-Fe spinel: Performance, mechanism and kinetic study. *Appl. Catal. B Environ.* **2011**, *110*, 71–80. [[CrossRef](#)]
28. Fan, Z.Y.; Shi, J.W.; Gao, C.; Gao, G.; Wang, B.R.; Niu, C.M. Rationally designed porous MnO_x-FeO_x nanoneedles for low-temperature selective catalytic reduction of NO_x by NH₃. *ACS Appl. Mater. Interfaces* **2017**, *9*, 16117–16127. [[CrossRef](#)]
29. Liu, Z.; Sun, G.X.; Chen, C.; Sun, K.; Zeng, L.Y.; Yang, L.Z.; Chen, Y.J.; Wang, W.H.; Liu, B.; Lu, Y.K.; et al. Fe-doped Mn₃O₄ spinel nanoparticles with highly exposed Fe_{oct}-O-Mn_{tet} sites for efficient selective catalytic reduction (SCR) of NO with ammonia at low temperatures. *ACS Catal.* **2020**, *10*, 6803–6809. [[CrossRef](#)]
30. Zhang, L.; Shi, L.Y.; Huang, L.; Zhang, J.P.; Gao, R.H.; Zhang, D.S. Rational design of high-performance DeNO_x catalysts based on Mn_xCo_{3-x}O₄ nanocages derived from metal-organic frameworks. *ACS Catal.* **2014**, *4*, 1753–1763. [[CrossRef](#)]
31. Zhu, W.J.; Tang, X.L.; Gao, F.Y.; Yi, H.H.; Zhang, R.C.; Wang, J.E.; Yang, C.; Ni, S.Q. The effect of non-selective oxidation on the Mn₂Co₁O_x catalysts for NH₃-SCR: Positive and non-positive. *Chem. Eng. J.* **2020**, *385*, 123797. [[CrossRef](#)]
32. Cai, S.X.; Zhang, D.S.; Shi, L.Y.; Xu, J.; Zhang, L.; Huang, L.; Li, H.R.; Zhang, J.P. Porous Ni-Mn oxide nanosheets in situ formed on nickel foam as 3D hierarchical monolith de-NO_x catalysts. *Nanoscale* **2014**, *6*, 7346–7353. [[CrossRef](#)]
33. Wan, Y.P.; Zhao, W.R.; Tang, Y.; Li, L.; Wang, H.J.; Cui, Y.L.; Gu, J.L.; Li, Y.S.; Shi, J.L. Ni-Mn bi-metal oxide catalysts for the low temperature SCR removal of NO with NH₃. *Appl. Catal. B Environ.* **2014**, *148–149*, 114–122. [[CrossRef](#)]
34. Shi, Y.; Chu, Q.; Xiong, W.; Gao, J.S.; Huang, L.; Zhang, Y.Q.; Ding, Y. A new type bimetallic NiMn-MOF-74 as an efficient low-temperatures catalyst for selective catalytic reduction of NO by CO. *Chem. Eng. Process.* **2021**, *159*, 108232. [[CrossRef](#)]
35. Xu, H.; Zhang, Q.L.; Qiu, C.T.; Lin, T.; Gong, M.C.; Chen, Y.Q. Tungsten modified MnO_x-CeO₂/ZrO₂ monolith catalysts for selective catalytic reduction of NO_x with ammonia. *Chem. Eng. Sci.* **2012**, *76*, 120–128. [[CrossRef](#)]

36. Liu, L.J.; Su, S.; Chen, D.Z.; Shu, T.; Zheng, X.T.; Yu, J.Y.; Feng, Y.; Wang, Y.; Hu, S.; Xiang, J. Highly efficient NH₃-SCR of NO_x over MnFeW/Ti catalyst at low temperature: SO₂ tolerance and reaction mechanism. *Fuel* **2022**, *307*, 121805. [[CrossRef](#)]
37. Liu, Z.M.; Zhu, J.Z.; Li, J.H.; Ma, L.L.; Woo, S.I. Novel Mn-Ce-Ti mixed-oxide catalyst for the selective catalytic reduction of NO_x with NH₃. *ACS Appl. Mater. Interfaces* **2014**, *6*, 14500–14508. [[CrossRef](#)] [[PubMed](#)]
38. Jiang, H.X.; Wang, C.X.; Wang, H.Q.; Zhang, M.H. Synthesis of highly efficient MnO_x catalyst for low-temperature NH₃-SCR prepared from Mn-MOF-74 template. *Mater. Lett.* **2016**, *168*, 17–19. [[CrossRef](#)]
39. Yao, H.Y.; Cai, S.X.; Yang, B.; Han, L.P.; Wang, P.L.; Li, H.R.; Yan, T.T.; Shi, L.Y.; Zhang, D.S. In situ decorated MOF-derived Mn-Fe oxides on Fe mesh as novel monolithic catalysts for NO_x reduction. *New J. Chem.* **2020**, *44*, 2357–2366. [[CrossRef](#)]
40. Chen, R.Y.; Fang, X.Y.; Li, Z.G.; Liu, Z.M. Selective catalytic reduction of NO_x with NH₃ over a novel MOF-derived MnO_x catalyst. *Appl. Catal. A Gen.* **2022**, *643*, 118754. [[CrossRef](#)]
41. Ren, Z.Y.; Fan, H.; Wang, R. A novel ring-like Fe₂O₃-based catalyst: Tungstophosphoric acid modification, NH₃-SCR activity and tolerance to H₂O and SO₂. *Catal. Commun.* **2017**, *100*, 71–75. [[CrossRef](#)]
42. Ren, Z.Y.; Teng, Y.F.; Zhao, L.Y.; Wang, R. Keggin-tungstophosphoric acid decorated Fe₂O₃ nanoring as a new catalyst for selective catalytic reduction of NO_x with ammonia. *Catal. Today* **2017**, *297*, 36–45. [[CrossRef](#)]
43. Geng, Y.; Xiong, S.C.; Li, B.; Peng, Y.; Yang, S.J. Promotion of H₃PW₁₂O₄₀ grafting on NO_x abatement over γ-Fe₂O₃. Performance and reaction mechanism. *Ind. Eng. Chem. Res.* **2018**, *57*, 13661–13670. [[CrossRef](#)]
44. Wu, J.H.; Jin, S.L.; Wei, X.D.; Gu, F.J.; Han, Q.; Lan, Y.X.; Qian, C.L.; Li, J.Q.; Wang, X.R.; Zhang, R.; et al. Enhanced sulfur resistance of H₃PW₁₂O₄₀-modified Fe₂O₃ catalyst for NH₃-SCR: Synergistic effect of surface acidity and oxidation ability. *Chem. Eng. J.* **2021**, *412*, 128712. [[CrossRef](#)]
45. Weng, X.L.; Dai, X.X.; Zeng, Q.S.; Liu, Y.; Wu, Z.B. DRIFT studies on promotion mechanism of H₃PW₁₂O₄₀ in selective catalytic reduction of NO with NH₃. *J. Colloid Interf. Sci.* **2016**, *461*, 9–14. [[CrossRef](#)] [[PubMed](#)]
46. Geng, Y.; Xiong, S.C.; Li, B.; Liao, Y.; Xiao, X.; Yang, S.J. H₃PW₁₂O₄₀ grafted on CeO₂: A high-performance catalyst for the selective catalytic reduction of NO_x with NH₃. *Ind. Eng. Chem. Res.* **2018**, *57*, 856–866. [[CrossRef](#)]
47. Geng, Y.; Jin, K.; Mei, J.; Su, G.Y.; Ma, L.; Yang, S.J. CeO₂ grafted with different heteropoly acids for selective catalytic reduction of NO with NH₃. *J. Hazard. Mater.* **2020**, *382*, 121032. [[CrossRef](#)]
48. Putluru, S.S.R.; Mossin, S.; Riisager, A.; Fehrmann, R. Heteropoly acid promoted Cu and Fe catalysts for the selective catalytic reduction of NO with ammonia. *Catal. Today* **2011**, *176*, 292–297. [[CrossRef](#)]
49. Putluru, S.S.R.; Jensen, A.D.; Riisager, A.; Fehrmann, R. Heteropoly acid promoted V₂O₅/TiO₂ catalysts for NO abatement with ammonia in alkali containing flue gases. *Catal. Sci. Technol.* **2011**, *1*, 631–637. [[CrossRef](#)]
50. Tang, X.L.; Wang, C.Z.; Gao, F.Y.; Zhang, R.C.; Shi, Y.R.; Yi, H.H. Acid modification enhances selective catalytic reduction activity and sulfur dioxide resistance of manganese-cerium-cobalt catalysts: Insight into the role of phosphotungstic acid. *J. Colloid Interf. Sci.* **2021**, *603*, 291–306. [[CrossRef](#)]
51. Xiao, X.; Sheng, Z.Y.; Yang, L.; Dong, F. Low-temperature selective catalytic reduction of NO_x with NH₃ over a manganese and cerium oxide/graphene composite prepared by a hydrothermal method. *Catal. Sci. Technol.* **2016**, *6*, 1507–1514. [[CrossRef](#)]
52. Gao, F.Y.; Tang, X.L.; Yi, H.H.; Li, J.Y.; Zhao, S.Z.; Wang, J.G.; Chu, C.; Li, C.L. Promotional mechanisms of activity and SO₂ tolerance of Co- or Ni-doped MnO_x-CeO₂ catalysts for SCR of NO_x with NH₃ at low temperature. *Chem. Eng. J.* **2017**, *317*, 20–31. [[CrossRef](#)]
53. Meng, D.M.; Zhan, W.C.; Guo, Y.; Guo, Y.L.; Wang, L.; Lu, G.Z. A highly effective catalyst of Sm-MnO_x for the NH₃-SCR of NO_x at low temperature: Promotional role of Sm and its catalytic performance. *ACS Catal.* **2015**, *5*, 5973–5983. [[CrossRef](#)]
54. Jalil, P.A.; Faiz, M.; Tabet, N.; Hamdan, N.M.; Hussain, Z. A study of the stability of tungstophosphoric acid, H₃PW₁₂O₄₀, using synchrotron XPS, XANES, hexane cracking, XRD, and IR spectroscopy. *J. Catal.* **2003**, *217*, 292–297. [[CrossRef](#)]
55. Essayem, N.; Holmqvist, A.; Gayraud, P.Y.; Vedrine, J.C.; Taarit, Y.B. In situ FTIR studies of the protonic sites of H₃PW₁₂O₄₀ and its acidic cesium salts M_xH_{3-x}PW₁₂O₄₀. *J. Catal.* **2001**, *197*, 273–280. [[CrossRef](#)]
56. Jiang, Y.; Liu, T.Y.; Gao, W.Q.; Ge, H.W.; Yang, Z.D.; Lin, R.Y.; Wang, X.W. Three-dimensionally ordered macroporous Ce-W-Nb oxide catalysts for selective catalytic reduction of NO with NH₃. *Chem. Eng. J.* **2022**, *433*, 134576. [[CrossRef](#)]
57. Zhang, X.; Liu, Y.X.; Deng, J.G.; Zhao, X.T.; Zhang, K.F.; Yang, J.; Han, Z.; Jiang, X.Y.; Dai, H.X. Three-dimensionally ordered macroporous Cr₂O₃-CeO₂: High-performance catalysts for the oxidative removal of trichloroethylene. *Catal. Today* **2020**, *339*, 200–209. [[CrossRef](#)]
58. Lian, Z.H.; Liu, F.D.; He, H.; Shi, X.Y.; Mo, J.S.; Wu, Z.B. Manganese-niobium mixed oxide catalyst for the selective catalytic reduction of NO_x with NH₃ at low temperatures. *Chem. Eng. J.* **2014**, *250*, 390–398. [[CrossRef](#)]
59. Sun, P.; Guo, R.T.; Liu, S.M.; Wang, S.X.; Pan, W.G.; Li, M.Y. The enhanced performance of MnO_x catalyst for NH₃-SCR reaction by the modification with Eu. *Appl. Catal. A Gen.* **2017**, *531*, 129–138. [[CrossRef](#)]
60. Xiong, S.C.; Peng, Y.; Wang, D.; Huang, N.; Zhang, Q.F.; Yang, S.J.; Chen, J.J.; Li, J.H. The role of the Cu dopant on a Mn₃O₄ spinel SCR catalyst: Improvement of low-temperature activity and sulfur resistance. *Chem. Eng. J.* **2020**, *387*, 124090. [[CrossRef](#)]
61. Wu, X.; Liu, L.L.; Liu, J.N.; Hou, B.H.; Du, Y.L.; Xie, X.M. NiMn mixed oxides with enhanced low-temperature deNO_x performance: Insight into the coordinated decoration of MnO_x by NiO phase *via* glycine combustion method. *Appl. Catal. A Gen.* **2021**, *610*, 117918. [[CrossRef](#)]
62. Xiong, S.C.; Liao, Y.; Xiao, X.; Dang, H.; Yang, S.J. Novel effect of H₂O on the low temperature selective catalytic reduction of NO with NH₃ over MnO_x-CeO₂: Mechanism and kinetic study. *J. Phys. Chem. C* **2015**, *119*, 4180–4187. [[CrossRef](#)]

63. Wang, C.Z.; Gao, F.Y.; Ko, S.J.; Liu, H.H.; Yi, H.H.; Tang, X.L. Structural control for inhibiting SO₂ adsorption in porous MnCe nanowire aerogel catalysts for low-temperature NH₃-SCR. *Chem. Eng. J.* **2022**, *434*, 134729. [CrossRef]
64. Chen, L.Q.; Yuan, F.L.; Li, Z.B.; Niu, X.Y.; Zhu, Y.J. Synergistic effect between the redox property and acidity on enhancing the low temperature NH₃-SCR activity for NO removal over the Co_{0.2}Ce_xMn_{0.8-x}Ti₁₀ (x = 0–0.40) oxides catalysts. *Chem. Eng. J.* **2018**, *354*, 393–406. [CrossRef]
65. Kim, M.J.; Youn, J.R.; Lee, S.J.; Ryu, I.S.; Nam, S.C.; Jeong, S.K.; Jeon, S.K. Facile control of surface properties in CeO₂-promoted Mn/TiO₂ catalyst for low-temperature selective catalytic reduction of NO by NH₃. *J. Ind. Eng. Chem.* **2022**, *108*, 438–448. [CrossRef]
66. Yoon, W.; Kim, Y.; Kim, G.J.; Kim, J.-R.; Lee, S.; Han, H.; Park, G.H.; Chae, H.-J.; Kim, W.B. Boosting low temperature De-NO_x performance and SO₂ resistance over Ce-doped two dimensional Mn-Cr layered double oxide catalyst. *Chem. Eng. J.* **2022**, *434*, 134676. [CrossRef]
67. Chen, L.; Yao, X.J.; Cao, J.; Yang, F.M.; Tang, C.J.; Dong, L. Effect of Ti⁴⁺ and Sn⁴⁺ co-incorporation on the catalytic performance of CeO₂-MnO_x catalyst for low temperature NH₃-SCR. *Appl. Surf. Sci.* **2019**, *476*, 283–292. [CrossRef]
68. Zhang, Y.P.; Li, G.B.; Wu, P.; Zhuang, K.; Shen, K.; Wang, S.; Huang, T.J. Effect of SO₂ on the low-temperature denitrification performance of Ho-modified Mn/Ti catalyst. *Chem. Eng. J.* **2020**, *400*, 122597. [CrossRef]
69. Li, C.X.; Shen, M.Q.; Yu, T.; Wang, J.Q.; Wang, J.; Zhai, Y.P. The mechanism of ammonium bisulfate formation and decomposition over V/W/Ti catalysts for NH₃-selective catalytic reduction at various temperatures. *Phys. Chem. Chem. Phys.* **2017**, *19*, 15194–15206. [CrossRef]
70. Xiong, Z.B.; Wang, W.; Li, J.; Huang, L.H.; Lu, W. The synergistic promotional effect of W doping and sulfate modification on the NH₃-SCR activity of CeO₂ catalyst. *Mol. Catal.* **2022**, *522*, 112250. [CrossRef]
71. Liu, Y.P.; He, B.; Li, Q.; Liu, H.; Qiu, L.; Liu, J.; Xiang, W.; Liu, Y.X.; Wang, G.K.; Wu, Z.G.; et al. Relieving capacity decay and voltage fading of Li_{1.2}Ni_{0.13}Co_{0.13}Mn_{0.54}O₂ by Mg²⁺ and PO₄³⁻ dual doping. *Mater. Res. Bull.* **2020**, *130*, 110923. [CrossRef]
72. Li, Y.F.; Hou, Y.Q.; Zhang, Y.Z.; Yang, Y.T.; Huang, Z.G. Confinement of MnO_x@Fe₂O₃ core-shell catalyst with titania nanotubes: Enhanced N₂ selectivity and SO₂ tolerance in NH₃-SCR process. *J. Colloid Interf. Sci.* **2022**, *608*, 2224–2234. [CrossRef] [PubMed]
73. Xue, H.Y.; Guo, X.M.; Meng, T.; Guo, Q.S.; Mao, D.S.; Wang, S. Cu-ZSM-5 catalyst impregnated with Mn-Co oxide for the selected catalytic reduction of NO: Physicochemical property-catalytic activity relationship and in situ DRIFTS study for the reaction mechanism. *ACS Catal.* **2021**, *11*, 7702–7718. [CrossRef]
74. Liu, Y.Y.; Gao, F.Y.; Ko, S.J.; Wang, C.Z.; Liu, H.H.; Tang, X.L.; Yi, H.H.; Zhou, Y.S. Superior catalytic performance within H₂O-vapor of W-modified CoMn₂O₄/TiO₂ catalyst for selective catalytic reduction of NO_x with NH₃. *Chem. Eng. J.* **2022**, *434*, 134770. [CrossRef]
75. Fan, Z.Y.; Shi, J.W.; Gao, C.; Gao, G.; Wang, B.R.; Wang, Y.; He, C.; Niu, C.M. Gd-modified MnO_x for the selective catalytic reduction of NO by NH₃: The promoting effect of Gd on the catalytic performance and sulfur resistance. *Chem. Eng. J.* **2018**, *348*, 820–830. [CrossRef]
76. Gao, E.H.; Feng, W.J.; Huang, B.; Zhu, J.L.; Wang, W.; Li, J.W.; He, Y. The enhanced resistance to Na⁺-poisoning of MnCoCrO_x SCR catalyst by acidity regulation: The mechanism of sulfuric acid pretreatment. *Mol. Catal.* **2022**, *518*, 112084. [CrossRef]
77. Hu, H.; Cai, S.X.; Li, H.R.; Huang, L.; Shi, L.Y.; Zhang, D.S. In situ DRIFTS investigation of the low-temperature reaction mechanism over Mn-doped Co₃O₄ for the selective catalytic reduction of NO_x with NH₃. *J. Phys. Chem. C* **2015**, *119*, 22924–22933. [CrossRef]
78. Meng, D.M.; Xu, Q.; Jiao, Y.L.; Guo, Y.; Guo, Y.L.; Wang, L.; Lu, G.Z.; Zhan, W.C. Spinel structured Co_aMn_bO_x mixed oxide catalyst for the selective catalytic reduction of NO_x with NH₃. *Appl. Catal. B Environ.* **2018**, *221*, 652–663. [CrossRef]
79. Fan, A.D.; Jing, Y.; Guo, J.X.; Shi, X.K.; Yuan, S.D.; Li, J.J. Investigation of Mn doped perovskite La-Mn oxides for NH₃-SCR activity and SO₂/H₂O resistance. *Fuel* **2022**, *310*, 122237. [CrossRef]
80. Xu, Q.; Li, Z.Y.; Wang, L.; Zhan, W.C.; Guo, Y.L.; Guo, Y. Understand the role of redox property and NO adsorption over MnFeO_x for NH₃-SCR. *Catal. Sci. Technol.* **2022**, *12*, 2030–2041. [CrossRef]
81. Hu, H.; Cai, S.X.; Li, H.R.; Huang, L.; Shi, L.Y.; Zhang, D.S. Mechanistic aspects of deNO_x processing over TiO₂ supported Co-Mn oxide catalysts: Structure-activity relationships and in situ DRIFTS analysis. *ACS Catal.* **2015**, *5*, 6069–6077. [CrossRef]
82. Xue, H.Y.; Guo, X.M.; Meng, T.; Mao, D.S.; Ma, Z. NH₃-SCR of NO over M/ZSM-5 (M = Mn, Co, Cu) catalysts: An in-situ DRIFTS study. *Surf. Interfaces* **2022**, *29*, 101722. [CrossRef]
83. Qiu, L.; Pang, D.D.; Zhang, C.L.; Meng, J.J.; Zhu, R.S.; Ouyang, F. In situ IR studies of Co and Ce doped Mn/TiO₂ catalyst for low-temperature selective catalytic reduction of NO with NH₃. *Appl. Surf. Sci.* **2015**, *357*, 189–196. [CrossRef]
84. Guo, R.T.; Wang, S.X.; Pan, W.G.; Li, M.Y.; Sun, P.; Liu, S.M.; Sun, X.; Liu, S.W.; Liu, J. Different poisoning effects of K and Mg on the Mn/TiO₂ catalyst for selective catalytic reduction of NO_x with NH₃: A mechanistic study. *J. Phys. Chem. C* **2017**, *121*, 7881–7891. [CrossRef]
85. Xie, S.Z.; Li, L.L.; Jin, L.J.; Wu, Y.H.; Liu, H.; Qin, Q.J.; Wei, X.L.; Liu, J.X.; Dong, L.H.; Li, B. Low temperature high activity of M (M = Ce, Fe, Co, Ni) doped M-Mn/TiO₂ catalysts for NH₃-SCR and in situ DRIFTS for investigating the reaction mechanism. *Appl. Surf. Sci.* **2020**, *515*, 146014. [CrossRef]
86. Kijlstra, W.S.; Brands, D.S.; Poels, E.K.; Blik, A. Mechanism of the selective catalytic reduction of NO by NH₃ over MnO_x/Al₂O₃. I. Adsorption and desorption of the single reaction components. *J. Catal.* **1997**, *171*, 208–218. [CrossRef]

87. Wei, L.H.; Li, X.Y.; Mu, J.C.; Wang, X.Y.; Fan, S.Y.; Yin, Z.F.; Tadé, M.O.; Liu, S.M. Rationally tailored redox properties of a mesoporous Mn-Fe spinel nanostructure for boosting low-temperature selective catalytic reduction of NO_x with NH₃. *ACS Sustain. Chem. Eng.* **2020**, *8*, 17727–17739. [[CrossRef](#)]
88. Sun, Q.; Gao, Z.X.; Wen, B.; Sachtler, W.M.H. Spectroscopic evidence for a nitrite intermediate in the catalytic reduction of NO_x with ammonia on Fe/MFI. *Catal. Lett.* **2002**, *78*, 1–5. [[CrossRef](#)]
89. Gao, F.Y.; Tang, X.L.; Yi, H.H.; Zhao, S.Z.; Wang, J.E.; Gu, T. Improvement of activity, selectivity and H₂O & SO₂-tolerance of micro-mesoporous CrMn₂O₄ spinel catalyst for low-temperature NH₃-SCR of NO_x. *Appl. Surf. Sci.* **2019**, *466*, 411–424. [[CrossRef](#)]
90. Gao, F.Y.; Tang, X.L.; Yi, H.H.; Zhao, S.Z.; Wang, J.G.; Shi, Y.R.; Meng, X.M. Novel Co or Ni-Mn binary oxide catalysts with hydroxyl groups for NH₃-SCR of NO_x at low temperature. *Appl. Surf. Sci.* **2018**, *443*, 103–113. [[CrossRef](#)]